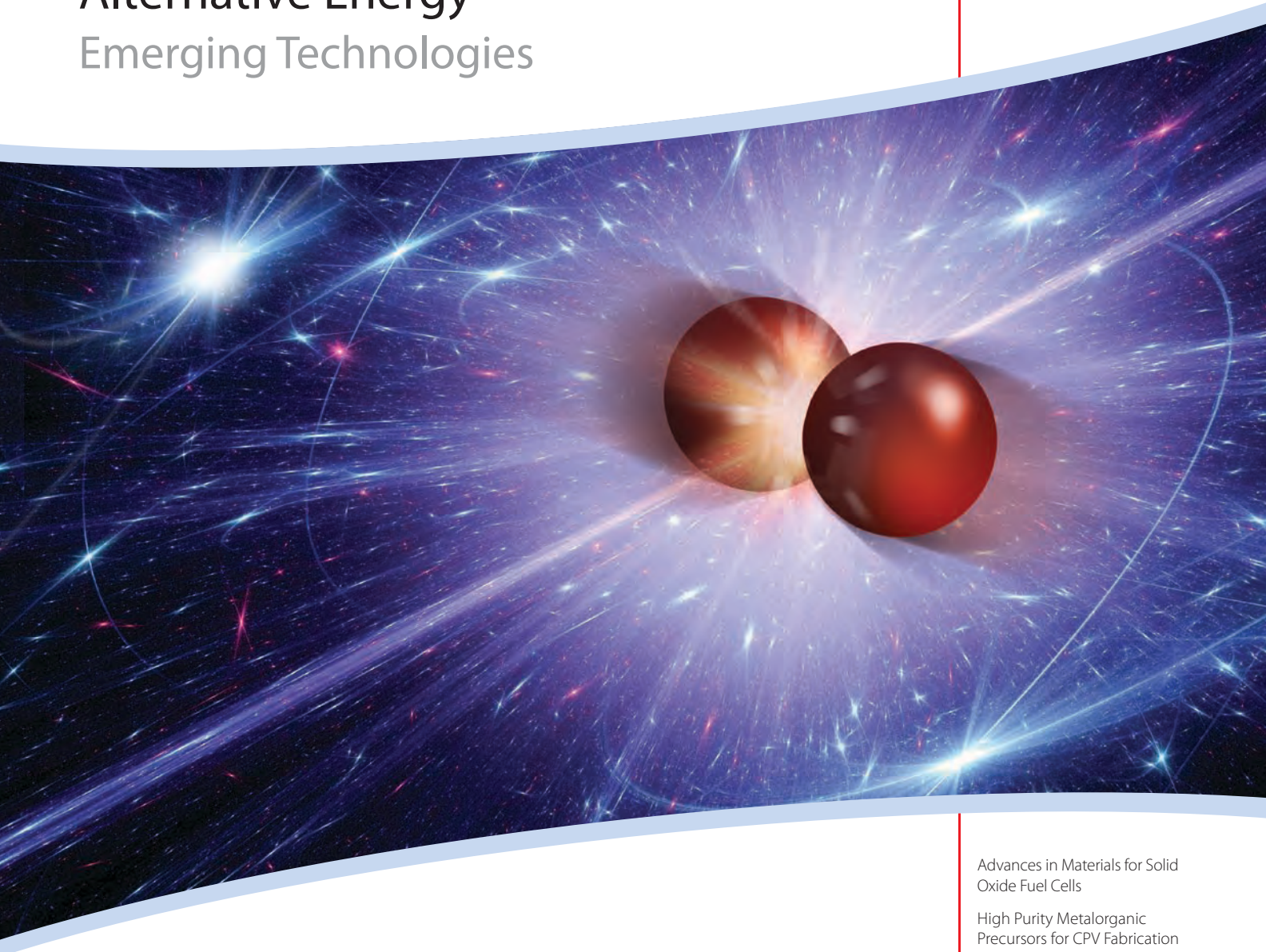


# Material Matters™

Volume 5, Number 4 • 2010



## Alternative Energy Emerging Technologies



*A New Power in Materials Science is Emerging*

Advances in Materials for Solid Oxide Fuel Cells

High Purity Metalorganic Precursors for CPV Fabrication

Complex Hydrides: New Lithium Conductors

Mechanochemical Effect of Severe Plastic Deformations

## Introduction

Welcome to the fourth and final installment of *Material Matters*<sup>™</sup> for 2010, focusing on emerging technologies for Alternative Energy applications. The term Alternative Energy encompasses a wide range of technologies aimed at replacing fossil fuels with clean renewable energy sources such as solar power, hydrogen, biomass, wind, and hydropower, as well as adjacent areas of energy storage in batteries, hydrogen-rich media and electrical charge storage devices.

Solar cells and photovoltaic (PV) modules, which convert solar radiation directly into electricity, represent one of the most attractive alternative approaches to electrical energy generation. Despite relatively high production costs, PV cells are becoming increasingly important, especially after recent discoveries of new high-performance materials comprised of multi-junction thin film systems.<sup>1</sup>

Solid Oxide Fuel Cells (SOFCs) represent another approach to energy generation by producing electricity through the oxidation of hydrogen or carbon monoxide. The recent progress in the development of new SOFC materials has led to an overall reduction in costs for the electricity generated using these fuel cells and turned them into a viable energy source for a variety of stationary applications. In addition, since SOFCs have high optimum operating temperatures, ranging from 773 K to 1,273 K,<sup>2</sup> the heat produced during their operation can be utilized in conventional gas turbines, thus increasing the efficiency of the entire system to 70-75%.<sup>3</sup>

The hydrogen required for different types of fuel cells can be generated remotely and saved in an appropriate form for later use. Metal hydrides represent one of the safest and most efficient ways to store hydrogen.<sup>4</sup> The ability of hydrogen absorbers to interact with gaseous hydrogen often depends on the manufacturing technique used for their preparation. A technique that has been widely used in the preparation of metallic hydrogen storage media is mechanical alloying, which produces high-surface area metal alloys with extremely high affinities towards hydrogen.

It is worth noting that the use of metal hydrides for energy applications is not limited to hydrogen storage only. For example, lithium borohydride-based composites have proved to be quite efficient solid ion conductors with potential applications in Li-ion batteries and related devices.

In this issue of *Material Matters*, we feature four articles highlighting emergent technologies for alternative energy applications and the materials that are central to these studies. To begin, Raymond Gorte (University of Pennsylvania) discusses current state-of-the-art SOFC materials as well as promising areas of development toward next generation devices with superior thermal and mechanical stabilities. Simon Rushworth (SAFC Hitech<sup>®</sup> Limited) describes the fabrication of multi-junction PV cells by Metal Organic Vapor Phase Epitaxy (MOVPE). Researchers from Tohoku University report their discovery of lithium fast-ion conduction in LiBH<sub>4</sub>, providing a basis for further studies of complex metal hydrides as electrolytes for all-solid-state Li-ion batteries. Finally, Jacques Huot from the Hydrogen Research Institute and Viktor Balema from Sigma-Aldrich<sup>®</sup> discuss the role of severe plastic deformation in the preparation of hydrogen storage material by mechanical processing as well as chemical transformations facilitated in solid materials by mechanical milling, grinding, or cold rolling.

Each article in this publication is accompanied by a list of relevant materials available from Aldrich<sup>®</sup> Materials Science. For additional product information, please visit Aldrich Materials Science at [aldrich.com/matsci](http://aldrich.com/matsci). If you have any comments or questions regarding *Material Matters* or would like to suggest a product, please contact us at [matsci@sial.com](mailto:matsci@sial.com).

### References

- (1) Rushworth, S. *Material Matters* **2010**, Vol. 5, No. 4, 94.
- (2) Gorte, R. J. *Material Matters* **2010**, Vol. 5, No. 4, 90.
- (3) (a) Ormerod, R.M. *Chem. Soc. Rev.* **2003**, 32, 17. (b) Tubular Solid Oxide Fuel Cell Technology. U.S. Department of Energy. [http://www.fossil.energy.gov/programs/powersystems/fuelcells/fuelcells\\_solidoxide.html](http://www.fossil.energy.gov/programs/powersystems/fuelcells/fuelcells_solidoxide.html) (accessed Oct 12, 2010).
- (4) Karkamkar, A.; Aardahl, C.; Autrey, T. *Material Matters* **2007**, Vol. 2, No. 2, 6.

## About Our Cover

The development of new materials with enhanced physical and chemical properties is essential for the continued advancement of alternative energy technologies. Included among these technologies are fuel cells (p. 90), photovoltaic devices (p. 94), rechargeable batteries (p. 105), and hydrogen storage materials (p. 112). Efforts to provide reliable, sustainable sources of power generation and energy storage are often collaborative, multidisciplinary approaches, combining varying areas of knowledge and expertise. The cover art represents the birth of new ideas from the collision of scientific disciplines in the pursuit of alternative energy solutions.



Nathan Henderson  
Materials Science  
Sigma-Aldrich Corporation

## Material Matters<sup>™</sup>

Vol. 5, No. 4 • 2010

Aldrich Chemical Co., Inc.  
Sigma-Aldrich Corporation  
6000 N. Teutonia Ave.  
Milwaukee, WI 53209, USA

### To Place Orders

Telephone 800-325-3010 (USA)  
FAX 800-325-5052 (USA)

### Customer & Technical Services

Customer Inquiries 800-325-3010  
Technical Service 800-231-8327  
SAFC<sup>®</sup> 800-244-1173  
Custom Synthesis 800-244-1173  
Flavors & Fragrances 800-227-4563  
International 414-438-3850  
24-Hour Emergency 414-438-3850  
Website [sigma-aldrich.com](http://sigma-aldrich.com)  
Email [aldrich@sial.com](mailto:aldrich@sial.com)

### Subscriptions

To request your FREE subscription to *Material Matters*, please contact us by:

Phone: 800-325-3010 (USA)  
Mail: Attn: Marketing Communications  
Aldrich Chemical Co., Inc.  
Sigma-Aldrich Corporation  
P.O. Box 2988  
Milwaukee, WI 53201-2988  
Website: [sigma-aldrich.com/mm](http://sigma-aldrich.com/mm)  
Email: [sams-usa@sial.com](mailto:sams-usa@sial.com)

International customers, please contact your local Sigma-Aldrich office. For worldwide contact information, please see back cover.

*Material Matters* is also available in PDF format on the Internet at [aldrich.com/matsci](http://aldrich.com/matsci).

Aldrich brand products are sold through Sigma-Aldrich, Inc. Sigma-Aldrich, Inc. warrants that its products conform to the information contained in this and other Sigma-Aldrich publications. Purchaser must determine the suitability of the product for its particular use. See reverse side of invoice or packing slip for additional terms and conditions of sale.

All prices are subject to change without notice.

*Material Matters* (ISSN 1933-9631) is a publication of Aldrich Chemical Co., Inc. Aldrich is a member of the Sigma-Aldrich Group. © 2010 Sigma-Aldrich Co.

## "Your Materials Matter"

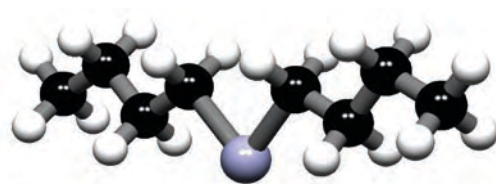


*Joe Porwoll*

Joe Porwoll, President  
Aldrich Chemical Co., Inc.

Do you have a compound that you wish Sigma-Aldrich® could list to help materials research? If it is needed to accelerate your research, it matters—please send your suggestion to [matsci@sial.com](mailto:matsci@sial.com) and we will be happy to give it careful consideration.

Professor Torben Jensen of the University of Aarhus in Denmark kindly suggested that we offer a solution of di-*n*-butyl magnesium (Aldrich Prod. No. 731110) as a material for energy storage applications. Dibutyl magnesium can be used to generate MgH<sub>2</sub>, a hydrogen storage material, through thermal decomposition<sup>1</sup> and through reaction with hydrogen, phenylsilane, or other reducing agents.<sup>2</sup> This compound can also serve as a deposition precursor for both elemental Mg on Pt as well as MgH<sub>2</sub> into nanoporous carbon frameworks.<sup>3,4</sup> Finally, di-*n*-butyl magnesium finds use as polymerization initiators<sup>5</sup> and in organic synthesis.<sup>6,7</sup>



### Di-*n*-butylmagnesium solution

[1191-47-5] BRN 3535184  
[CH<sub>3</sub>(CH<sub>2</sub>)<sub>3</sub>]<sub>2</sub>Mg FW 138.53



#### ► 1 M in ether and hexanes

density.....0.736 g/mL, 25 °C

[731110-100ML](#)

100 mL

### References

- (1) Allendorf, M.D. 2009, U.S. Department of Energy, [http://www.hydrogen.energy.gov/pdfs/review09/stp\\_48\\_allendorf.pdf](http://www.hydrogen.energy.gov/pdfs/review09/stp_48_allendorf.pdf) (accessed Oct. 15, 2010).
- (2) Michalczuk, M. *Organometallics* **1992**, *11*, 2307.
- (3) Viestfried, Y.; Levi, M.D.; Gofer, Y.; Aurbach, D. *J. Ele. Chem.* **2005**, *576*, 183.
- (4) Zhang, S.; Gross, A.F.; Van Atta, S.L.; Maribel, L.; Liu, P.; Ahn, C.C.; Vajo, J.J.; Jensen, C.M. *Nanotechnol.* **2009**, *20*, 204027.
- (5) Wurm, B.; Keul, H.; Höker H.; Sylvester, G.; Leitz, E.; Ott, K.-H. *Makromol. Chem., Rapid Commun.* **1992**, *13*, 9.
- (6) Screttas, C.G. and Steele, B.R. *J. Organomet. Chem.* **1986**, *317*, 137.
- (7) Duff, A.W.; Hitchcock, P.B.; Lappert, M.F.; Taylor, R.G.; Segal, J.A. *J. Organomet. Chem.* **1985**, *293*, 271.

## Alternative Energy Materials Featured in this Issue

Materials Category	Content	Page
Solid Oxide Fuel Cell Electrolyte Materials	Cerium(IV) oxide and Zirconium(IV) oxide based products for use as electrolytes in SOFCs	92
Solid Oxide Fuel Cell Electrode Materials	A selection of complex metal oxide materials for use as electrodes in SOFCs	93
Metal Oxides for SOFC Applications	A selection of transition metal oxides suitable for the preparation of materials for SOFC applications	93
Stainless Steel Bubblers	A select list of bubblers for use with Atomic Layer Deposition (ALD) and Chemical Vapor Deposition (CVD) systems	100
Aldrich® Precursors Packaged for Deposition Systems	Metal Organic Precursors precursors packaged for use in Atomic Layer Deposition (ALD) and Chemical Vapor Deposition (CVD) systems	100
Aldrich Materials Suitable for Vapor Deposition of Thin Films	Metal Organic precursors for Atomic Layer Deposition (ALD) and Chemical Vapor Deposition (CVD)	101
Battery Electrolyte Materials: Ionic Liquids and Solvents	A selection of ionic liquids and solvents for battery applications	108
Lithium Salts for Energy Applications: Hydrides and Amides	Lithium hydride and amide products suitable for Li-ion battery applications	109
Lithium Salts for Energy Applications: Halogenides	Lithium halogenides suitable for designing advanced electrolytes for Li-ion battery applications	110
Metal Hydrides for Hydrogen Storage Applications	A select list of metal hydrides with particular use in hydrogen storage systems	115
Metal Alloys for Hydrogen Storage	A list of metallic hydrogen absorbers with applications in hydrogen storage and batteries	116
High Purity Magnesium	A selection of high-purity magnesium materials for hydrogen storage	116

## Advances in Materials for Solid Oxide Fuel Cells



Raymond J. Gorte  
Chemical & Biomolecular Engineering  
University of Pennsylvania,  
Philadelphia, PA 19104  
Email: gorte@seas.upenn.edu

### Introduction

As with all types of fuel cells, a Solid Oxide Fuel Cell (SOFC) is capable of efficiently transforming chemical energy into electrical energy. However, unlike fuel cells based on proton-conducting electrolytes, SOFCs are not limited to using  $H_2$  as the fuel and can in principle operate on any combustible fuel, including carbon monoxide,<sup>1</sup> hydrocarbons,<sup>2</sup> and even coal.<sup>3</sup> SOFCs are based on ceramic membranes that are oxygen-ion conductors and operate according to the principles shown in **Figure 1**.  $O_2$  from the air is reduced to  $O^{2-}$  anions at the cathode, and the anions are then transported through the electrolyte membrane to the anode where the fuel is oxidized.

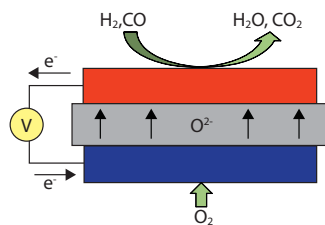


**Figure 1.** Schematic of SOFC operating on  $H_2$  or  $CO$ .

None of the known oxides that are used as electrolytes show significant ionic conductivity below 773 K; therefore SOFCs must operate at relatively high temperatures, from 773 K to 1,273 K. Unfortunately, high temperatures can result in materials challenges and much of the research in SOFC has been aimed at allowing operation at the lower end of the temperature range. High temperatures, however, provide a number of important advantages. They allow the activation of molecules like  $O_2$  at the cathode and  $CH_4$  at the anode with small electrode losses (i.e., low overpotentials). Heat management is also much easier at high temperatures. In any fuel cell, the chemical energy that is not converted to electrical energy is given up as heat. This heat can be used by endothermic reforming reactions in an SOFC; even if it is to simply be discarded, heat transfer to ambient is much easier in an SOFC. Traditionally, the view has been that SOFC would be used only in large-scale power generation, but this is no longer true. Although high temperatures represent challenges for small-scale applications, portable SOFC for applications such as battery replacements and microchip power sources are being developed industrywide.

In an ideal fuel cell, the potential of the produced electrons would be increased by an amount determined from the Nernst Equation (**Equation 1**), a thermodynamic expression that relates the change in the voltage of the electrons to the change in the Gibbs Free Energy of the reaction.

$$V_{\text{Nernst}} = V^{\circ} + \frac{RT}{nF} \ln \left( \frac{P_{H_2, \text{anode}} \cdot P_{O_2, \text{cathode}}^{\frac{1}{2}}}{P_{H_2O, \text{anode}}} \right) \quad (1)$$

Indeed, in the absence of current flow, SOFCs closely approach equilibrium and the open-circuit voltage (OCV) can be used to measure the difference in chemical potentials across the electrolyte. This is the basis for oxygen sensors used in today's automobiles.<sup>4</sup> However, current must be allowed to flow in order to produce energy, and losses in the electrodes and the electrolyte will cause the cell potential to decrease. For example, since the electrolyte has a resistance that can be calculated from its thickness and resistivity, the potential loss in the electrolyte is  $iR_E$ , where  $i$  is the current density in  $A/cm^2$  and  $R_E$  is the resistance in  $\Omega \cdot cm^2$ . The relationship between current density and overpotential losses in the cathode,  $\eta_{\text{cathode}}$ , and anode,  $\eta_{\text{anode}}$ , may be complex. Finally, the operating potential of the cell,  $V$ , will be given by **Equation 2**:

$$V = V_{\text{Nernst}} - (i \cdot R_E + \eta_{\text{cathode}} + \eta_{\text{anode}}) \quad (2)$$

Unlike low-temperature fuel cells such as Proton Exchange Membrane (PEM) fuel cells, where the cell potential usually decreases exponentially with current density near open circuit, the relationship between cell potential and current density is often linear in SOFCs. When the relationship is linear, the losses in the anode and cathode can be described by their impedances,  $R_{\text{anode}}$  and  $R_{\text{cathode}}$  (effectively the resistances of those components). A typical goal for fuel cell developers is to have the total cell impedance be less than  $0.3 \Omega \cdot cm^2$ , the impedance required to achieve a power density of  $1 W/cm^2$ . Since the cathode, electrolyte, and anode form a circuit in series, the losses from each component are additive, so that each component should have an impedance less than  $\sim 0.1 \Omega \cdot cm^2$ .<sup>5</sup>

### Materials in the Present State-of-the-Art SOFCs

The composition of SOFCs presently under development has not changed dramatically in the last 30 years. The most commonly used electrolyte is still yttria-stabilized zirconia (YSZ, **Aldrich Prod. No. 544779**). Although there are oxides that have higher ionic conductivities, YSZ is relatively inexpensive and has negligible electronic conductivity under even the most reducing conditions. At 973 K, the losses associated with a  $10 \mu m$  YSZ electrolyte are only  $0.05 \Omega \cdot cm^2$ . Anodes are typically porous composites of Ni and YSZ. The Ni provides electronic conductivity and catalytic activity, while the YSZ provides channels for ionic conduction within the electrode, helps maintain porosity, and helps match the coefficients of thermal expansion between the electrode and electrolyte. Because cathodes must maintain good electronic conductivity at high temperatures in air, the main component is almost always a conductive oxide, Sr-doped  $LaMnO_3$  (LSM, **Aldrich Prod. No. 704296**). As with the anode, LSM is often mixed with YSZ to form a cathode composite (**Aldrich Prod. No. 704245**).



Although this set of materials has not changed much since 1975,<sup>6</sup> there have been a number of advances that have greatly lowered the operating temperature, from ~1,273 K to below 1,073 K, and have brought commercialization closer. The first of these was the development of anode-supported cells.<sup>7</sup> While the exact fabrication details vary, these cells are prepared from a bilayer green body with a relatively thick film (~500  $\mu\text{m}$ ) made from a physical mixture of NiO (Aldrich Prod. No. 481793) and YSZ powders and a thinner film (~10  $\mu\text{m}$ ) of YSZ powder. Since NiO and YSZ do not form solid solutions, this bilayer can be sintered to high enough temperatures to form a dense electrolyte from the YSZ layer. After applying the cathode to the dense YSZ (i.e., by screen printing a mixture of LSM and YSZ powders), the NiO-YSZ composite (Aldrich Prod. No. 704202) is reduced to form the porous Ni-YSZ anode. In addition to the fact that this procedure results in a thin electrolyte, the co-firing of the anode and electrolyte forms an anode-electrolyte interface that is nearly ideal for promoting the electrochemical reactions. Cathode performance usually limits performance in these cells.

The second major advance has been in the use of cathodes made from Mixed Ionic and Electron Conducting (MIEC) perovskites, such as Sr-doped  $\text{LaCo}_{0.2}\text{Fe}_{0.8}\text{O}_3$  (LSCF, Aldrich Prod. No. 704288).<sup>8</sup> While LSM has high electronic conductivity, its oxygen-ion conductivity is negligible—only  $10^6$  times that of YSZ. By comparison, LSCF has ionic conductivity that is only about 50 times lower than that of YSZ, while maintaining high electronic conductivity. The increased ionic conductivity widens the three-phase boundary, the electrochemically active zone where gas-phase  $\text{O}_2$  can react with electrons to form oxygen ions. The difficulty with LSCF is that it readily undergoes solid-state reactions with YSZ. To avoid this problem, a micron-size thin layer of doped-ceria (Aldrich Prod. No. 572357) is introduced as an interlayer between the LSCF and the YSZ in order to prevent solid-state reactions.<sup>8</sup>

## Materials for the Future

Although the electrodes in the present materials set work reasonably well, there are a number of issues that could be improved using new formulations and fabrication methods. First, replacement of the Ni-YSZ composite (Aldrich Prod. No. 704229) at the anode would open up the possibility of using hydrocarbon fuels without the need for reforming. As discussed at the beginning of the article, it is theoretically possible to fuel an SOFC with almost any combustible fuel. Unfortunately, Ni catalyzes the formation of carbon fibers from carbon hydrides, which can deactivate the cell and cause stresses that lead to its fracture or loss of Ni via corrosion known as “metal dusting”. By replacing Ni with Cu or a conducting ceramic, the SOFC can operate directly on methane and even liquid fuels.<sup>1,2</sup>

The problem with Ni-anode replacements has been that their anode impedances have been too high, requiring significantly higher temperatures to achieve similar power densities to those achieved with SOFC based on Ni-YSZ anodes. The impaired performance is partially due to the fact that one cannot use the co-sintering process that is used with anode-supported cells to achieve the nearly ideal electrode-electrolyte structure. Essentially all materials that could be used to replace Ni undergo solid-state reactions with YSZ at the temperatures needed to form a dense electrolyte layer.

A very promising solution to the problem of obtaining a good interface with alternative materials involves infiltration of the active electrode components into a porous layer of the electrolyte, as shown schematically in Figure 2.

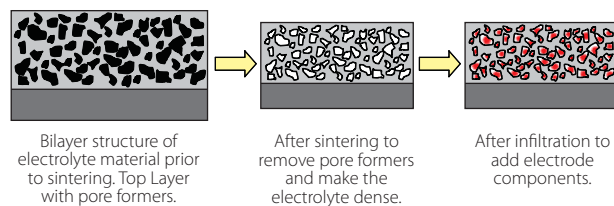


Figure 2. Diagram of the procedure for fabricating SOFC by infiltration.

The first step is fabrication of a porous YSZ layer on a dense YSZ electrolyte. This porous-dense bilayer is most easily prepared by tape casting, with sacrificial pore formers introduced on one side of the initial green body; however, at least one study started with a Ni-YSZ, anode-supported cell and removed the Ni by etching in nitric acid, which leaves the YSZ unaffected. Next, materials for providing electronic conductivity and catalytic activity are infiltrated into the porous layer using solution-phase chemistry. The catalyst and the electronic conductor can be the same material, as it is with Ni-YSZ anodes, or two separate materials can be used to serve these functions. For example, studies have shown excellent performance using a ceramic conductor ( $\text{La}_{0.8}\text{Sr}_{0.2}\text{Cr}_{0.5}\text{Mn}_{0.5}\text{O}_3$ , LSCM) with dopant levels of Ni, Pd, or Pt.<sup>9</sup>

In addition to improved materials flexibility, lower temperatures can be used in the processing of infiltrated electrodes, so that solid-state reactions can be avoided. Furthermore, because the mechanical properties of composites formed by infiltration are determined by the YSZ scaffold, which has been fired to very high temperatures together with the YSZ electrolyte, these composites exhibit superior mechanical properties. Finally, it seems possible to engineer interactions between the electrode material and the electrolyte that lead to intrinsic electrode stability.<sup>10</sup>

The preparation of composites by infiltration also shows great promise for improved cathodes.<sup>5</sup> In addition to providing a nearly ideal, electrode-electrolyte interface and lower processing temperatures, the infiltration procedure produces a non-random composite, since the material added for electronic conduction is introduced after the porous electrolyte structure has been established. The importance of having a non-random structure is two-fold. Firstly, less of the electronic conductor is required to provide good conductivity since this phase essentially coats the pores and is therefore well connected. Secondly, there is less need to match the coefficients of thermal expansion in the non-random composite, since the electrolyte scaffold in the porous composite primarily determines the mechanical properties. This allows electrode materials to be chosen primarily for their electrochemical performance.

Another promising area for SOFC involves fabrication of thin layers of the active SOFC components onto a porous metal support structure.<sup>11</sup> The porous metal can be relatively inexpensive since it is used only for mechanical strength and current collection. The use of a metal support greatly simplifies the sealing of the cells and provides good mechanical strength, along with resistance to thermal shock. The materials used for the SOFC components can be essentially anything, although the processing conditions must be compatible with maintaining the metal support. Because most inexpensive metals, such as stainless steel, cannot tolerate high-temperature sintering in air, the use of infiltration procedures for preparing the cathodes can be very valuable.

## Direct-carbon Fuel Cells

There has been significant interest in the development of fuel cells which can generate electrical power from solid fuels, such as coal and biomass.<sup>12,13</sup> The challenge here is to develop materials that would allow transfer of the oxygen ions from the electrolyte to the surface of the solid fuel. One approach is to use CO<sub>2</sub> to oxidize the solid fuel, forming CO, which is subsequently oxidized on the SOFC anode. This can be used with SOFCs based on the traditional materials. However, SOFCs based on molten anodes would seem to offer an approach that is more generally applicable to all carbonaceous fuels, no matter how easily they are oxidized by CO<sub>2</sub>.

The most studied of the molten anodes uses a molten carbonate mixture (e.g., Li<sub>2</sub>CO<sub>3</sub> + K<sub>2</sub>CO<sub>3</sub> + Na<sub>2</sub>CO<sub>3</sub>) as the liquid anode to transfer oxygen ions from the ceramic electrolyte to the fuel. The molten carbonates have been shown to efficiently oxidize carbonaceous fuels that are immersed in them; however, they are not electrically conductive. This lack of electronic conductivity requires incorporation of a metallic current collector immersed in the highly corrosive molten-carbonate solution. A more serious problem is that oxidation by CO<sub>3</sub><sup>2-</sup> ions, in addition to CO<sub>2</sub>. As a result, the performance of these electrodes is limited by slow transfer of electrons from the site of solid-fuel surface to the metallic current collector. A possible solution to this problem involves using a conductive form of carbon as fuel and maintaining a high concentration of that carbon within the carbonate. While this approach has resulted in impressive performance (>100 mW/cm<sup>2</sup> at 785 °C for operation on coal<sup>12</sup>), it limits what fuels can be used, since the fuel itself is part of the anode.

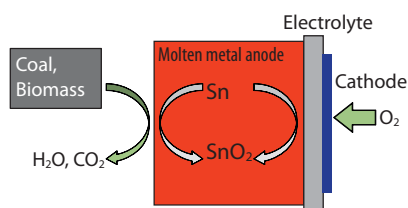


Figure 3. Schematic of a Direct-Carbon Fuel Cell using a molten Sn anode.

Another approach to achieving fuel cells that operate on carbon involves using molten-metal anodes.<sup>7-9</sup> In this approach, oxygen from the electrolyte is transferred to the molten metal to form the metal oxide, as shown in Figure 3, which is subsequently reduced by the fuel, either in the anode compartment itself or by removing the oxygen-saturated metal and reducing it in a separate reactor. Implementation of this strategy is under way with molten Sn anodes.<sup>13</sup> Other molten metals are also under consideration.<sup>14</sup>

## Summary

Although SOFC and solid oxide electrolyzers (SOE) are still in early stages of development, the performance that has already been achieved shows that this technology has great promise for conversion between chemical and electrical energy.

## Acknowledgments

This work was supported by the U.S. Department of Energy's Hydrogen Fuel Initiative (grant DE-FG02-05ER15721).

## References

- (1) Bidrawn, F.; Kim, G.; Corre, G.; Irvine, J. T. S.; Vohs, J. M.; Gorte, R. J. *Electrochem. Sol-State Lett.*, **2008**, *11*, B167.
- (2) Park, S.; Vohs, J. M.; Gorte, R. J. *Nature*, **2000**, *404*, 265.
- (3) Homel, M.; Gur, T. M.; Koh, J. H.; Virkar, A. V. *J. Power Sources*, **2010**, *195*, 6367.
- (4) Riegel, J.; Neumann, H.; Wiedenmann, H.-M. *Solid State Ionics*, **2002**, *152*, 783.
- (5) Vohs, J. M.; Gorte, R. J. *Ad. Matls.*, **2009**, *21*, 943.
- (6) Minh, N. Q.; *J. Am. Ceram. Soc.*, **1993**, *76*, 563.
- (7) Kim, J.-W.; Virkar, A. V.; Fung, K.-Z.; Mehta, K.; Singhal, S. C. *J Electrochem. Soc.*, **1999**, *146*, 69.
- (8) Haanappel, V. A. C.; Mertens, J.; Mai, A. *J. Fuel Cell Sci. Techn.*, **2006**, *3*, 263.
- (9) Kim, J.-S.; Nair, V. V.; Vohs, J. M.; Gorte, R. J. *Scripta Materialia*, **2010**, doi:10.1016/j.scriptamat.2010.06.016.
- (10) Kim, G.; Corre, G.; Irvine, J. T. S.; Vohs, J. M.; Gorte, R. J. *Electrochem & Sol-State Lett.*, **2008**, *11*, B16.
- (11) Tucker, M. C. *J. Power Sources*, **2010**, *195*, 4570.
- (12) Nabae, Y.; Pointon, K. D.; Irvine, J. T. S. *Energy & Environ. Sci.*, **2008**, *1*, 148.
- (13) McPhee, W. A. G.; Boucher, M.; Stuart, J.; Parnas, R. S.; Koslowski, M.; Tao, T.; Wilhite, B. A. *Energy Fuels*, **2009**, *23*, 5036.
- (14) Jayakumar, A.; Vohs, J. M.; Gorte, R. J. *Ind. Engin. Chem. Res.*, **2010**, doi:10.1021/ie100457t.

## Solid Oxide Fuel Cell Electrolyte Materials

For a complete list of available SOFC electrolytes, please visit [aldrich.com/energy](http://aldrich.com/energy)

Name	Additives	Particle Size	Surface Area	Prod. No.
Cerium(IV) oxide-calcium doped	calcium 10 mol % as dopant	<100 nm	100-120 m <sup>2</sup> /g	572403-25G
Cerium(IV) oxide-gadolinium doped	gadolinium 10 mol % as dopant	<100 nm	>100 m <sup>2</sup> /g	572330-25G
Cerium(IV) oxide-gadolinium doped	gadolinium 20 mol % as dopant	<100 nm	>100 m <sup>2</sup> /g	572357-25G
Cerium(IV) oxide-samarium doped	samarium 15 mol % as dopant	<100 nm	100-120 m <sup>2</sup> /g	572365-25G
Cerium(IV) oxide-yttria doped	yttria 15 mol % as dopant	<100 nm	100-120 m <sup>2</sup> /g	572381-25G
Zirconium(IV) oxide-yttria stabilized	yttria 3 mol % as stabilizer	≤100 nm	100-120 m <sup>2</sup> /g	572322-25G
Zirconium(IV) oxide-yttria stabilized	yttria ~5.3 mol % as stabilizer	~500 nm	6.9 m <sup>2</sup> /g	464201-100G 464201-500G
Zirconium(IV) oxide-yttria stabilized	yttria 8 mol % as stabilizer	≤100 nm	>100 m <sup>2</sup> /g	572349-25G
Zirconium(IV) oxide-yttria stabilized	yttria ~8 mol % as stabilizer	~700 nm	5.5 m <sup>2</sup> /g	464228-100G 464228-500G
Zirconium(IV) oxide-yttria stabilized	yttria 0-10 mol % as stabilizer	<100 nm (BET)	40-60 m <sup>2</sup> /g (BET)	544779-25G

## Solid Oxide Fuel Cell Electrode Materials

For a complete list of available SOFC electrodes, please visit [aldrich.com/energy](http://aldrich.com/energy)

Name	Description	Composition	Prod. No.
Lanthanum strontium cobalt ferrite	LSCF 6428	$\text{La}_{0.6}\text{Sr}_{0.4}\text{Co}_{0.2}\text{Fe}_{0.8}\text{O}_3$	704288-10G
Lanthanum strontium cobalt ferrite	LSCF/GDC composite cathode powder	$(\text{Ce}_{0.9}\text{Gd}_{0.1})\text{O}_{1.95}$ 50 wt. % $(\text{La}_{0.60}\text{Sr}_{0.40})(\text{Co}_{0.20}\text{Fe}_{0.80})\text{O}_3$ 50 wt. %	704253-10G
Lanthanum strontium manganite	LSM-20	$(\text{La}_{0.80}\text{Sr}_{0.20})\text{MnO}_3$	704296-10G
Lanthanum strontium manganite	LSM-35	$\text{La}_{0.65}\text{Sr}_{0.35}\text{MnO}_3$	704261-10G
Lanthanum strontium manganite	LSM-20/GDC10 composite cathode powder	$(\text{La}_{0.80}\text{Sr}_{0.20})_{0.95}\text{MnO}_3$ 50 wt. % $\text{Ce}_{0.9}\text{Gd}_{0.1}\text{O}_{1.95}$ 50 wt. %	704237-10G
Lanthanum strontium manganite	LSM-20/YSZ composite cathode powder	$(\text{La}_{0.80}\text{Sr}_{0.20})\text{MnO}_3$ 50 wt. % $(\text{Y}_2\text{O}_3)_{0.08}(\text{ZrO}_2)_{0.92}$ 50 wt. %	704245-10G
Nickel oxide - Cerium samarium oxide	NiO/SDC for coatings	Cerium Samarium Oxide 40 wt. % Nickel Oxide 60 wt. %	704210-10G
Nickel oxide - Ytria-stabilized zirconia	NiO/YSZ general applications	Nickel Oxide 60 wt. % Ytria-stabilized Zirconia 40 wt. %	704229-10G
Nickel oxide - Ytria-stabilized zirconia	NiO/YSZ for coatings	Nickel Oxide 66 wt. % Ytria-stabilized zirconia 34 wt. %	704202-10G

## Metal Oxides for SOFC Applications

For a complete list of available metal oxides, please visit [aldrich.com/energy](http://aldrich.com/energy)

Name	Linear Formula	Description	Form	Prod. No.
Cerium(IV) oxide	$\text{CeO}_2$	>99.95% trace metals basis, particle size <50 nm (BET)	nanopowder	700290-25G 700290-100G
Cerium(IV) oxide	$\text{CeO}_2$	99.995% trace metals basis	powder	202975-10G 202975-50G
Cerium(IV) oxide	$\text{CeO}_2$	99.9% trace metals basis, <5 $\mu\text{m}$	powder	211575-100G 211575-500G
Cerium(IV) oxide	$\text{CeO}_2$	99.9% trace metals basis, 3 - 6 mm	fused pieces	342955-50G
Cerium(IV) oxide	$\text{CeO}_2$	$\geq 99.0\%$	solid	22390-100G-F 22390-500G-F
Cerium(IV) oxide	$\text{CeO}_2$	particle size <25 nm (BET)	nanopowder	544841-5G 544841-25G
Cerium(IV) oxide	$\text{CeO}_2$	90%	powder	348341-100G
Cerium(IV) oxide, dispersion	$\text{CeO}_2$	avg. part. size 10 - 20 $\mu\text{m}$	dispersion	289744-100G 289744-500G
Cerium(IV) oxide, dispersion	$\text{CeO}_2$	particle size <25 nm	dispersion nanoparticles	643009-100ML 643009-250ML
Cerium(IV)-zirconium(IV) oxide	$(\text{CeO}_2)_x(\text{ZrO}_2)_y$	99.0% trace metals basis, particle size <50 nm (BET)	nanopowder	634174-25G 634174-100G
Nickel(II) oxide	$\text{NiO}$	99.999% trace metals basis	solid	481793-5G 481793-25G
Nickel(II) oxide	$\text{NiO}$	99.99% trace metals basis	powder and chunks	203882-20G 203882-100G
Nickel(II) oxide	$\text{NiO}$	99.8% trace metals basis, particle size <50 nm (BET)	nanopowder	637130-25G 637130-100G 637130-250G
Nickel(II) oxide	$\text{NiO}$	99%, -325 mesh	powder	399523-100G
Strontium oxide	$\text{SrO}$	99.9% trace metals basis	powder	415138-10G 415138-50G
Strontium peroxide	$\text{SrO}_2$	-	powder	415200-100G
Vanadium(III) oxide	$\text{V}_2\text{O}_3$	99.99% trace metals basis	powder and chunks	463744-5G 463744-25G
Vanadium(V) oxide	$\text{V}_2\text{O}_5$	99.99% trace metals basis	powder	204854-1G 204854-5G 204854-25G
Yttrium(III) oxide	$\text{Y}_2\text{O}_3$	99.999% trace metals basis	powder	204927-10G 204927-50G
Yttrium(III) oxide	$\text{Y}_2\text{O}_3$	99.99% trace metals basis	powder	205168-10G 205168-50G 205168-250G
Yttrium(III) oxide	$\text{Y}_2\text{O}_3$	particle size <50 nm	nanopowder	544892-25G
Yttrium(III) oxide, dispersion	$\text{Y}_2\text{O}_3$	$\geq 99.9\%$ trace metals basis, particle size <50 nm (XRD) particle size <100 nm (BET)	nanoparticles	641901-25ML 641901-100ML
Yttrium(III) oxide, dispersion	$\text{Y}_2\text{O}_3$	$\geq 99.9\%$ trace metals basis, <100 nm (DLS)	dispersion nanoparticles	702048-100G

# High Purity Metalorganic Precursors for CPV Device Fabrication



Simon Rushworth  
SAFC Hitech Limited, Sigma-Aldrich Corporation  
Power Road, Bromborough, Wirral, UK CH62 3QF  
Email: simon.rushworth@sial.com

## Introduction

Thin film photovoltaic devices have become increasingly important in efficiently harnessing solar energy to meet consumer demand. Conventional crystalline silicon solar cells have demonstrated remarkably improved performance in recent years, but still suffer from a range of natural limitations on efficiency, prompting the development of new materials to allow further advances. To date, the highest conversion efficiencies have been demonstrated using III-V compound semiconductors, and efforts are underway to integrate these materials into next generation architectures in a cost effective way. The high price of raw materials is of particular concern so thin film and concentrator photovoltaic technologies (CPV) are being targeted to reduce the quantity of the expensive semiconductor material required (for a given module size and power output).

To allow operation of miniature devices with reduced surface area and materials volume, highly advanced structures of the highest quality are required. The most attractive fabrication technique for III-V compound semiconductor layers is Metal Organic Vapor Phase Epitaxy (MOVPE). The control of composition stoichiometries, layer thicknesses and interface roughness achievable using MOVPE is key to minimize internal losses and increase overall conversion efficiencies. The demanding operating conditions (500 - 1,000 suns) place extreme stress on the device structure. Precise deposition of active layers, window/buffer layers and conducting oxide and/or metal electrode layers must be attained to maximize performance.

Selection and use of the appropriate chemical precursors is critical in the achievement of the highest quality layers using MOVPE. These materials must be of the highest purity and must be supplied to the deposition chamber in a uniform manner. This article discusses some of the issues related to the use of these precursors.

## High Concentration CPV Multijunction Solar Cells

In a single band gap solar cell structure, such as those used in conventional crystalline silicon devices, one active layer is present to absorb photons. The conversion efficiency of the complete device is limited by the inability of this active material to absorb all of the photons impacting the device due to their broad range of energies. Photons with energies below the band gap of the active layer are lost because they are unable to provide sufficient energy to promote an electron to the required energy state and therefore pass through the layer unaffected. Photons with higher energies transfer only the energy required to perform the excitation and electron-hole pair generation for current extraction, with the remaining excess energy converted to heat. According to theoretical calculations, the maximum power conversion of a single band gap solar cell at standard conditions [AirMass (AM) 1.5] is about 30%.<sup>1</sup> Conventional technologies are already reaching 23%, suggesting that further improvements will be increasingly difficult to achieve without a change in approach.

By utilizing multiple junction solar cell designs with several different band gap materials, different portions of the solar spectrum may be converted at each junction, thus resulting in a cumulative effect leading to greater overall device efficiency. **Figure 1** illustrates the combined use of three cells in a multijunction cell that match the incident spectral irradiation with the absorbing capabilities of the complete device structure.<sup>2</sup> By modifying the individual layer compositions, improved matching of the absorption characteristics of the different sections can be achieved to increase the overall device photon capture capabilities. Beneficial changes can be made to the band gap engineering to customize cell properties for optimum performance in a particular region. These advances have led to a consistent improvement in device efficiencies.

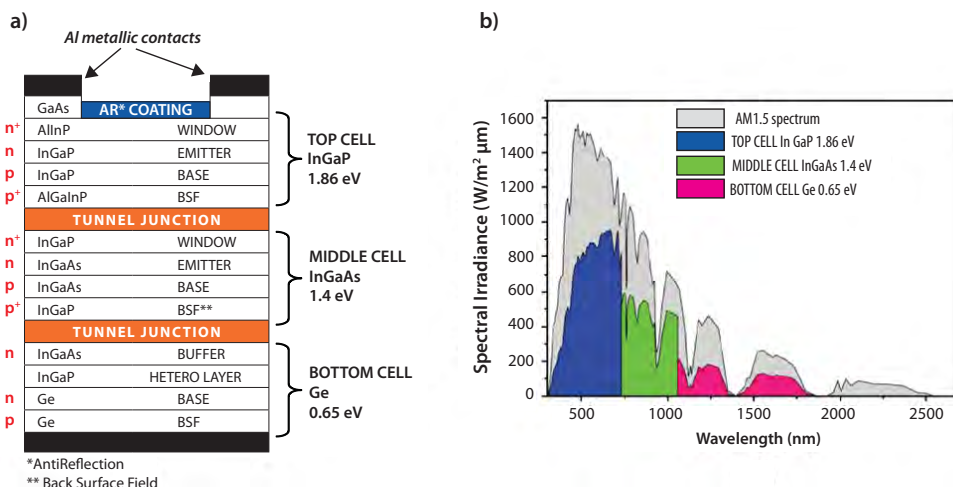
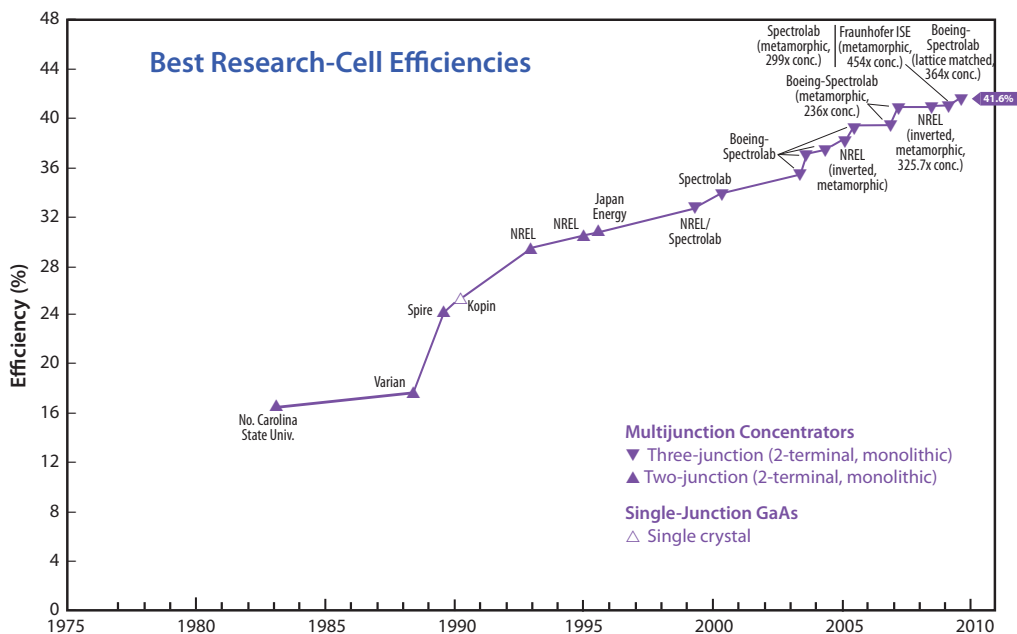


Figure 1. Multijunction solar cell (a) layer structure (b) spectral absorption.



The operation of the III-V multijunction device demonstrates improved performance when the impinging light is highly focused, hence mirrors and lenses are employed to concentrate light onto the device up to 500 - 1,000 sun energy levels. These concentrator photovoltaic (CPV) devices have been studied intensely in recent years, and the advances

demonstrated in both materials performance and concentrator technologies over the last decade have been significant, as shown in **Figure 2**.<sup>2</sup> The current record efficiency for a three-junction, lattice-matched GaInP/GaInAs (1.4 eV)/Ge cell is 41.6%.<sup>3</sup>



**Figure 2.** Historic summary of champion cell efficiencies for various photovoltaic technologies.<sup>2</sup>

Cell efficiencies have been increasing at a rate of about 0.5% to 1% per year and are expected to continue to increase toward 45% - 50% at the same pace. The implementation of additional cells in multijunction devices has been predicted to raise ideal values for 3-, 4-, and 5-junction cells to 47.3%, 49.3% and 50.5%, respectively.<sup>4</sup> It should also be noted that, as concentrator technologies improve, the use of light falling on a larger area can be converted by the same size active multijunction cell as previously employed. This scaling anomaly means that more electricity can be generated per unit volume of the expensive semiconductor to reduce cost. Coupled with the higher conversion efficiency at higher illumination concentrations to further increase output, CPV is clearly very promising as a next generation power generation technology.

## MOVPE Process

The basic MOVPE process was first demonstrated in the 1970s for GaAs thin film formation. Since then, the fundamentals have not changed, although the complexity of layer compositions and combinations has increased dramatically. MOVPE differs from the more generic Metal Organic Chemical Vapor Deposition (MOCVD) technique only in the nature of the films deposited. MOCVD encompasses amorphous, polycrystalline and epitaxial films, while MOVPE focuses solely on the epitaxial films. The technique involves passing vapors containing the individual components required for the target film into a deposition chamber containing a heated substrate. The vapors flow over the substrate and are thermally decomposed to deposit a coating, with the by-products swept away from the surface by the carrier gas (**Figure 3**). By changing the precursor-supply ratios, films with different stoichiometries can be deposited. The control of this process is the key factor in the production of advanced devices.

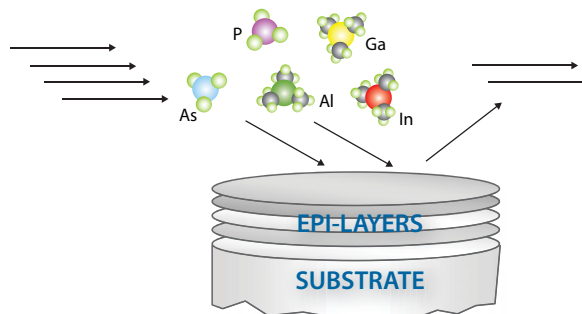


**Figure 3.** Illustration of MOVPE process.

The generation of precursor vapors is achieved by passing a carrier gas through the liquid or solid chemical reservoir. Saturating the gas stream is desired so that the precise uptake of precursor into the gas phase is constant per unit volume, even when changing flow rates. A known amount of chemical is then delivered to the deposition chamber by controlling the volume of this saturated gas. To achieve constant saturation levels, the design of the precursor container has been modified, as described later in this article.

MOVPE of compound semiconductors employs highly reactive, toxic and pyrophoric precursors, which present numerous challenges to handling, purification and use. The main products employed for Group III metal sources are trimethyl derivatives; namely Trimethylgallium ( $\text{Me}_3\text{Ga}$ , TMGa), Trimethylaluminum ( $\text{Me}_3\text{Al}$ , TMA) and Trimethylindium ( $\text{Me}_3\text{In}$ , TMIIn). The Group V sources employed are hydrides; namely Arsine ( $\text{AsH}_3$ ) and Phosphine ( $\text{PH}_3$ ). The thorough mixing of precursor vapors in the chamber and minimization of interactions between them to form particles, has been optimized so that highly uniform films can be deposited.

In today's process tools, multiple substrates are coated in each deposition run. Complex holders are employed that rotate during the run to increase the uniformity of the deposited layer over the whole of the substrate area. This motion also improves reproducibility between wafers and batches. These advanced technologies enable the fabrication of large numbers of devices for inclusion into solar cell modules for increased installed power generation. In comparison with Molecular Beam Epitaxy (MBE), which can also produce some of the complex III-V structures needed, MOVPE is more cost effective.

## III-V Compound Semiconductor Precursor Purity

The structure of the complete cell must be as perfect as possible, as the active components are under highly demanding conditions. Similarly, to avoid unwanted internal losses due to non-radiative centers and the generation of excessive heat, the number of metallic contaminants must be exceptionally low. This stipulation demands ultra-high precursor purities to avoid contaminant introduction with the vapors passed into the reaction chamber. Proprietary processes must be employed to isolate final chemicals with sub-ppm impurity concentrations and strict handling protocols must be employed to avoid contamination prior to introduction to the substrate. Significant experience in the area of III-V semiconductor high brightness LED production can be accessed to provide chemicals of the targeted quality in a manner suited to high volume usage with the degree of control required to afford the highest device performance.

In particular, it has been observed that oxygen (O) is an unwanted non-radiative center that detracts from cell operating efficiencies and lifetimes. To minimize O levels in the deposited films, the precursors used must be of the highest quality and, in particular, the organo-aluminum source must have contaminant levels less than 1 ppm.

Figure 4 shows the detected O species levels in a series of  $\text{Me}_3\text{Al}$  samples and Table 1 highlights the properties of aluminum gallium arsenide (AlGaAs) deposited using these samples. A direct correlation between the two sets of data is clearly seen, with contamination levels of less than 1 ppm in the source shown to be the key to achieving the highest final film quality.<sup>5</sup>

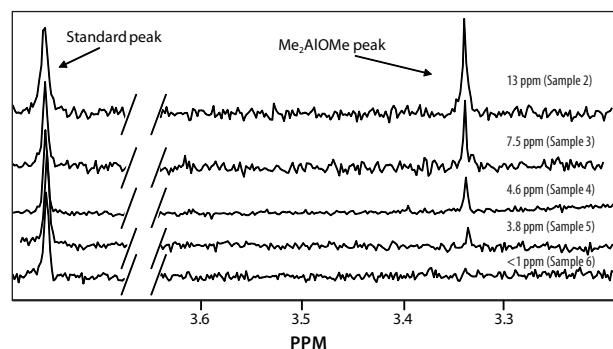


Figure 4. Proton NMR determination of -OMe content in different  $\text{Me}_3\text{Al}$  samples.

Table 1. Secondary Ion Mass Spectroscopy (SIMS) data for O impurity levels in MOVPE deposited AlGaAs films.

TMA Sample Number	O Level in TMA Using New NMR Technique	[O] in Al <sub>0.9</sub> Ga <sub>0.1</sub> As by SIMS (cm <sup>-3</sup> )		Composition
		p type (C) 3 - 5e18 cm <sup>-3</sup>	n type (Si) 1 - 3e18 cm <sup>-3</sup>	
Sample 1	>30 ppm	1 * 10 <sup>19</sup>	8 * 10 <sup>18</sup>	X=0.9
Sample 2	13 ppm	1 * 10 <sup>19</sup>	2 * 10 <sup>18</sup>	X=0.9
Sample 3	7.5 ppm	1.5 * 10 <sup>18</sup>	6 * 10 <sup>17</sup>	X=0.9
Sample 4	6.0 ppm	6 * 10 <sup>17</sup>	1.5 * 10 <sup>17</sup>	X=0.9
Sample 5	4.6 ppm	1 * 10 <sup>17</sup>	1 * 10 <sup>17</sup>	X=0.9
Sample 6	3.8 ppm	2 * 10 <sup>17</sup>	4 * 10 <sup>16</sup>	X=0.9
EpiPure™ TMA	<1 ppm (ND)	<3 * 10 <sup>16</sup> (ND)	<3 * 10 <sup>16</sup> (ND)	X=1

Also, at these ultra low contamination levels the equipment employed to perform the MOVPE growth must also be of the highest quality. Leak testing and surface pretreatments must be rigorously applied to ensure other O sources are minimized. For the trials performed, the batch to batch reproducibility of the state of the growth system employed was checked with repeat runs and a number of standard correlations to ensure the only variable was the Al precursor.

In a similar manner, direct correlation between metallic impurity levels, carrier numbers and carrier mobilities can be made, illustrating the need for complete removal of contaminants from sources employed in MOVPE.



## Precursor Vapor Transport

The delivery of a constant precursor gas phase concentration is critical to the development of MOVPE processes. To achieve the high levels of control necessary for the high quality films targeted, the supply must be stable over a wide range of operating conditions. In particular, interface abruptness is needed to avoid charge trapping and device degradation, and is highly dependant on precursor delivery control. To optimize the absorber efficiency, strict stoichiometric control of the alloy composition is critical and thus the vapor phase concentration of the precursors entering the growth chamber must be precisely metered, not only during one growth but over the lifetime of the chemical source. The vessel design has been studied intensively with a variety of approaches proposed in order to achieve the degree of reproducibility demanded. Initially, simple containers with a single diptube (bubblers) were employed, but as their volumes increased, the efficiency of vapor saturation was found to decrease towards the end of a batch. This drop off led to premature change out and lost production time. For liquids, a convenient solution for larger bubblers (>75 mm diameter) is the use of a cross dispersion arrangement at the end of the diptube. (Figure 5a) This device effectively spreads the carrier gas through the liquid, leading to complete vapor saturation over an extended fill level range, increasing the useable time for the source and reducing residual chemical at end of life.

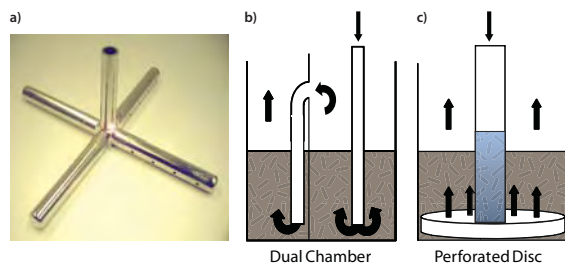


Figure 5. Improved pick up efficiency approaches (a) Cross diptube and (b) dual chamber (c) disc vessel.

The above methodology is not effective for solid precursors and more complex container geometries must be applied. The main objective of the container design is to increase the contact time between the carrier gas and the precursor to allow the most efficient vaporization possible. While it is relatively easy to achieve efficient vaporization with a full vessel, as the precursor is depleted, non-uniformities occur to form channels in the solid precursor where material has been removed. Gas passing through these channels has a reduced contact time with the precursor, leading to a drop in the vapor concentration achieved under identical flow conditions with a full vessel. To minimize the variance in precursor removal across the vessel cross section, several designs have been effectively demonstrated, including frit and perforated disc supports.<sup>6,7</sup> These supports ensure a laminar flow of gas passes through the solid. In combination with the use of multiple chambers, this provides much improved performance (Figures 5b and 5c). As batch volumes increase further, the requirement for innovative new vessels will again need attention to maximize the output stability of precursor vapors over the extended source lifetimes. This area remains one of the most challenging topics for industry scale-up and must be solved to allow true large area deposition of multijunction III-V devices required for commercialization.

Computer modeling is now being used to develop improved vessels, and typical data is shown in Figure 6 where gas flows are calculated (6a) and output fluxes generated (6b) for the most studied solid precursor,  $\text{Me}_3\text{In}$  (TMIn). It should be noted that the predicted stability and usage is a significant improvement on the state of the art, and initial testing of a prototype vessel has achieved these levels of output stability over an extended range of trial conditions.

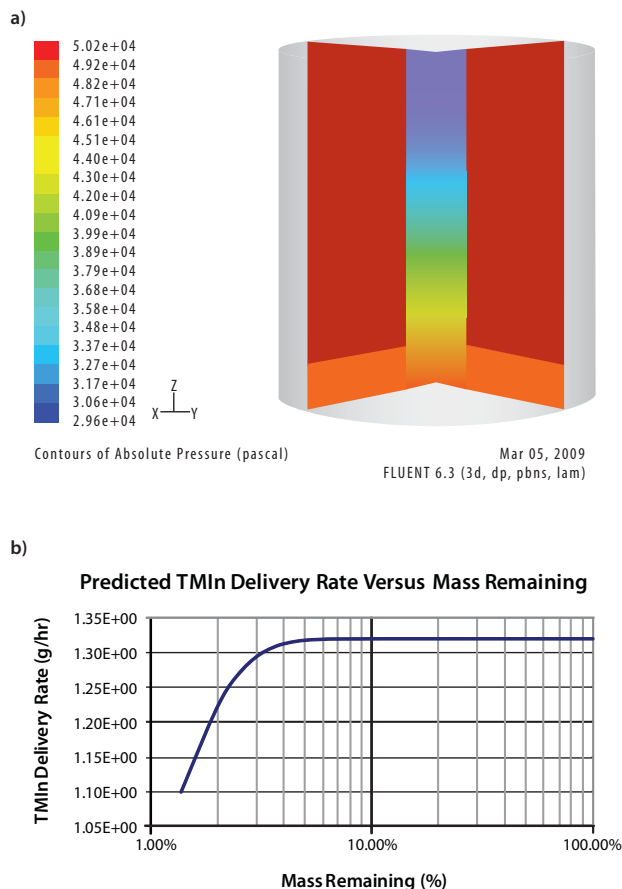
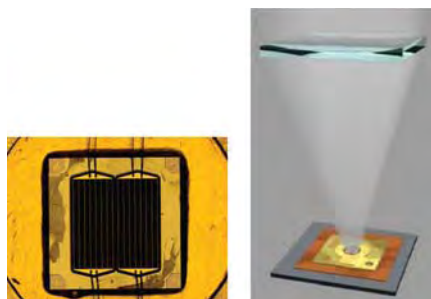


Figure 6. (a) Modelling of gas flows (b) output flux calculations for advanced vessel designs.

## High-efficiency CPV Device Example

Use of high purity metal organic precursors in a controlled fashion to fabricate precise layer structures has been an enabling technology for improved performance CPV devices. A recent example of a device from Fraunhofer ISE<sup>8</sup> with over 40% efficiency is illustrated in **Figure 7**. A three PN-junction combination of Gallium Indium Phosphide ( $\text{Ga}_{0.35}\text{In}_{0.65}\text{P}$ ), Gallium Indium Arsenide ( $\text{Ga}_{0.83}\text{In}_{0.17}\text{As}$ ) and Germanium (Ge) is employed. Absorption of sunlight across the ranges 300 - 780 nm, up to 1,020 nm and up to 1,880 nm is achieved by the different materials (**Figure 1b**), which has been predicted as particularly advantageous for optimizing conversion of the terrestrial solar spectrum to electricity.



**Figure 7.** Fraunhofer ISE high efficiency multijunction solar cell (a) active component (b) whole device.<sup>8</sup>

The solar cell has a cell area of 5.09 mm<sup>2</sup> and a 41.1% overall efficiency when operated at 454 suns. The ability to operate at even higher concentrations while maintaining high efficiency (37.6% @ C = 1,700) is a key advantage of this cell design, but this function is significantly dependant on perfect construction of all the individual layers and interfaces to avoid charge trapping and the more problematic defect propagation. The degradation of quality by such effects leads to reduced lifetimes, which are not acceptable in a commercial device. Hence, the focus on deposition technologies is to achieve high quality epitaxy throughout the multilayer structure. Similarly the impurity levels must be extremely low to avoid losses through heat generation. The ability to achieve close to theoretical outputs indicates that the materials employed were of the correct quality to ensure minimal contributions from this loss mechanism.

## Summary

The delivery of highly concentrated sunlight onto a very small-area, highly efficient (~40%) converter has the potential to provide a cost-effective approach to solar-electricity generation (especially in sunny locations). Fabrication of advanced thin film multijunction solar cells is moving towards large scale manufacture, and this industry is ready for substantial growth in the next years as the world enthusiastically embraces solar energy. MOVPE will be the technology of choice for production of these specialized cells, and the metal organic precursors employed need to be of the highest purity to maximize performance and enable robust, cost effective processes to be implemented to meet demand in this exciting field.

## References

- (1) Kurtz, S. Opportunities and Challenges for Development of a Mature Concentrating Photovoltaic Power Industry <http://www.nrel.gov/pv/pdfs/43208.pdf> (Accessed Oct. 5th 2010).
- (2) High-efficiency Multi-junction Solar Cells: Current Status and Future Potential. <http://sunlab.site.uottawa.ca/pdf/whitepapers/HIEfficMjSc-CurrStatus&FuturePotential.pdf> (Accessed Sept. 2010).
- (3) King, R.R.; Boca, A.; Hong, W.; Liu, X.-Q.; Bhusari, D.; Larrabee, D.; Edmondson, K.M.; Law, D.C.; Fetzer, C.M.; Mesropian, S.; Karam, N.H. 24th European Photovoltaic Solar Energy Conference and Exhibition, Hamburg, Germany, **2009**.
- (4) Araki, K.; Yamaguchi, M.; Kondo, M.; Uozumi, H. 3rd World Conference on PV Energy Conversion, **2003**, 307.
- (5) Rushworth, S.A.; Smith, L.M.; Ravetz, M.S.; Coward, K.M.; Odedra, R.; Kanjolia, R.; Bland, S.W.; Dimroth, F.; Bett, A.W. *J. Crystal Growth*, **2003**, 248, 86.
- (6) Shenai-Khatkhate, D.V.; DiCarlo, Jr., R.L.; Marsman, C.J.; Polcari, R.F.; Ware, R.A.; Woelk, E. *J. Crystal Growth*, **2007**, 298, 176.
- (7) Smith, L.M.; Odedra, R.; Kingsley, A.J.; Coward, K.M.; Rushworth, S.A.; Williams, Leese, T.A.; Purdie, A.J.; Kanjolia, R.K. *J. Crystal Growth*, **2004**, 272, 37.
- (8) Fraunhofer Institute for Solar Energie. [www.ise.fraunhofer.de](http://www.ise.fraunhofer.de) (Accessed Sept. 2010).

# SAFC Hitech<sup>®</sup> products for **CPV device manufacture** by MOVPE

SAFC Hitech, the global leader in specialty chemical supply to the semiconductor industry, supplies a range of products for CPV device fabrication by MOVPE. Its proprietary EpiPure™ Grade of products has been specifically designed for the high performance semiconductor device industry. State of the art analytical technologies are employed to guarantee ultra low impurity levels with sub ppm specifications for metals, organics and oxygen.

Name	Grade	Physical State	Order Code
Trimethylgallium (TMGa, Me <sub>3</sub> Ga)	EpiPure Grade	Liquid	TMGAEP
Trimethylaluminium (TMAI, Me <sub>3</sub> Al)	EpiPure Grade	Liquid	TMALEP
Trimethylindium (TMIn, Me <sub>3</sub> In)	EpiPure Grade	Solid	TMINEP
Solution TMI™ (TMIn, Me <sub>3</sub> In)	EpiPure Grade	Saturated solution	TMISEP
Triethylgallium (TEGa, Et <sub>3</sub> Ga)	EpiPure Grade	Liquid	TEGAEP
Bis(Cyclopentadienyl)Magnesium (Cp <sub>2</sub> Mg)	EpiPure Grade	Solid	CPMGEP
Solution Magnesiumocene (Cp <sub>2</sub> Mg)	EpiPure Grade	Saturated solution	CPMSEP
Carbon tetrabromide (CBr <sub>4</sub> )	EpiPure Grade	Solid	CBR4EP
Solution CBr <sub>4</sub> (CBr <sub>4</sub> )	EpiPure Grade	Saturated solution	CBRSEP
Diethylzinc (DEZn, Et <sub>2</sub> Zn)	EpiPure Grade	Liquid	DEZNEP

Visit the SAFC Hitech website for more information on these chemicals and details of how to contact us [safchitech.com](http://safchitech.com) or email [hitechinfo@sial.com](mailto:hitechinfo@sial.com).

Please use the SAFC Hitech Order Code for your inquiries for EpiPure Grade materials.

**SAFC** Hitech™  
Enabling Technology

[safchitech.com](http://safchitech.com)

SIGMA-ALDRICH®



## Stainless Steel Bubblers

Name	Capacity	Prod. No.
Stainless steel bubbler	100 mL	Z557870-1EA
Stainless steel bubbler	300 mL	Z527068-1EA
Stainless steel bubbler	1.2 L	Z553360-1EA

## Aldrich® Precursors Packaged for Deposition Systems

For a complete list of available deposition precursors, please visit [aldrich.com/deposition](http://aldrich.com/deposition)

Atomic Number of Base Material	Name (Synonym)	Structure	Physical State	Prod. No.
-	Water	$H_2O$	liquid	697125-25ML
13 Aluminum	Trimethylaluminum (TMA)		liquid	663301-25G
14 Silicon	(3-Aminopropyl)triethoxysilane (APTES)		liquid	706493-20ML
	Silicon tetrachloride (STC)	$SiCl_4$	liquid	688509-25ML
	Tris( <i>tert</i> -butoxy)silanol		solid	697281-25G
	Tris( <i>tert</i> -pentoxo)silanol (TPS)		liquid	697303-25G
22 Titanium	Tetrakis(diethylamido)titanium(IV) (TDEAT)		liquid	725536-10G
	Tetrakis(dimethylamido)titanium(IV) (TDMAT)		liquid	669008-25G
	Titanium tetrachloride (TTC)	$TiCl_4$	liquid	697079-25G
	Titanium(IV) isopropoxide	$[Ti(OCH(CH_3)_2)_4]^{4+}$	liquid	687502-25G
30 Zinc	Diethylzinc (DEZ)	$H_3C-CH_2-Zn-CH_2-CH_3$	liquid	668729-25G
31 Gallium	Triethylgallium (TEG)	$H_3C-CH_2-Ga-CH_2-CH_3$	liquid	730726-10G
	Trimethylgallium (TMG)	$H_3C-Ga-CH_3$	liquid	730734-10G
39 Yttrium	Tris( <i>N,N</i> -bis(trimethylsilyl)amide)yttrium		powder	702021-10G
40 Zirconium	Bis(methyl-η <sup>5</sup> -cyclopentadienyl)methoxymethylzirconium (ZRCMMM, ZrD-CO <sub>4</sub> )	$Zr(CH_3C_5H_4)_2CH_3OCH_3$	liquid	725471-10G
	Tetrakis(dimethylamido)zirconium(IV)		solid	669016-25G
	Tetrakis(ethylmethylamido)zirconium(IV)		liquid	725528-10G



Atomic Number of Base Material	Name (Synonym)	Structure	Physical State	Prod. No.
44 Ruthenium	Bis(ethylcyclopentadienyl) ruthenium(II)		liquid	679798-10G
72 Hafnium	Bis(methyl-η <sup>5</sup> -cyclopentadienyl) dimethylhafnium (HFCMME, HfD-CO <sub>2</sub> )	$\text{Hf}[\text{C}_5\text{H}_4(\text{CH}_3)]_2(\text{CH}_3)_2$	waxy solid	725501-10G
	Bis(methyl-η <sup>5</sup> -cyclopentadienyl) methoxymethylhafnium (HfD-CO <sub>4</sub> )	$\text{HfCH}_3(\text{OCH}_3)[\text{C}_5\text{H}_4(\text{CH}_3)]_2$	liquid	725498-10G
	Tetrakis(dimethylamido)hafnium(IV) (TDMAH)		low-melting solid	666610-25G
	Tetrakis(ethylmethylamido) hafnium(IV) (TEMAH)		liquid	725544-10G
73 Tantalum	Tris(diethylamido)(tert-butylimido) tantalum(V)		liquid	668990-10G
74 Tungsten	Bis(tert-butylimino)bis(dimethylamino)tungsten(VI)		liquid	668885-10G
78 Platinum	Trimethyl(methylcyclopentadienyl) platinum(IV)		low-melting solid	697540-10G

## Aldrich® Materials Suitable for Vapor Deposition of Thin Films

For a complete list of available thin film vapor deposition materials, please visit [aldrich.com/ald](http://aldrich.com/ald)

Atomic Number of Base Material	Name (Synonym)	Structure	Purity	Prod. No.
5 Boron	Boron trifluoride	$\text{BF}_3$	≥99.99%	463086-20G 463086-100G
	Diborane		9-11% (balance hydrogen) 99.99% (diborane only)	463051-48L
12 Magnesium	Bis(cyclopentadienyl)magnesium(II) (MgCp <sub>2</sub> )		≥95% ≥99.99% trace metals basis (excludes ~300 ppm Al)	J100042-10G
	Bis(pentamethylcyclopentadienyl) magnesium (MgCp* <sub>2</sub> )		99.999% trace metals basis	512540-1G
13 Aluminum	Tris(dimethylamido)aluminum(III)		-	469947-10G
14 Silicon	Disilane	$\text{H}_3\text{Si}-\text{SiH}_3$	99.998%	463043-20G
	Tetraethyl orthosilicate		99.999% trace metals basis	333859-25ML 333859-100ML
	Tetramethylsilane		≥99.99% trace metals basis	523771-100ML
15 Phosphorus	Phosphine	$\text{PH}_3$	≥99.9995%	295647-10G 295647-50G

Atomic Number of Base Material	Name (Synonym)	Structure	Purity	Prod. No.
20 Calcium	Calcium bis(6,6,7,7,8,8,8-heptafluoro-2,2-dimethyl-3,5-octanedionate)		≥99.9% trace metals basis	495158-5G
22 Titanium	Bis(diethylamido)bis(dimethylamido)titanium(IV)		≥99.99% trace metals basis ≥95%	J100026-10G
	Tetrakis(ethylmethylamido)titanium(IV)		≥99.99%	473537-5G 473537-8G
	Titanium(IV) methoxide	Ti(OCH <sub>3</sub> ) <sub>4</sub>	≥99.99% trace metals basis	463582-25G
23 Vanadium	Vanadyl acetylacetonate		99.99% trace metals basis	574562-5G
26 Iron	Iron(0) pentacarbonyl	Fe(CO) <sub>5</sub>	99.999% trace metals basis	481718-25ML 481718-100ML
	Iron(II) acetylacetonate		99.95% trace metals basis	413402-10G
	Iron(III) acetylacetonate		≥99.9% trace metals basis	517003-10G 517003-50G
27 Cobalt	Bis(ethylcyclopentadienyl)cobalt(II)		-	510645-1G 510645-5G
	Bis(pentamethylcyclopentadienyl)cobalt(II) (CoCp* <sub>2</sub> )		-	401781-1G
28 Nickel	Bis(ethylcyclopentadienyl)nickel(II)		-	510483-5G
29 Copper	Copper bis(2,2,6,6-tetramethyl-3,5-heptanedionate)		99%	345083-1G 345083-5G
	Germanium(IV) fluoride	GeF <sub>4</sub>	≥99.9%	463000-5G 463000-15G
32 Germanium	Tributylgermanium hydride		99%	409170-1G
	33 Arsenic	Triphenylarsine		99.99% trace metals basis
34 Selenium	Diethyl selenide	H <sub>3</sub> C-CH <sub>2</sub> -Se-CH <sub>2</sub> -CH <sub>3</sub>	99.999% trace metals basis	550434-5G 550434-25G
	Dimethyl selenide	H <sub>3</sub> C-Se-CH <sub>3</sub>	≥99.0%, GC	41572-1ML 41572-5ML
38 Strontium	Strontium tetramethylheptanedionate		99.9% trace metals basis	697524-1G
39 Yttrium	Tris(butylcyclopentadienyl)yttrium(III)		99.9% trace metals basis	524522-5ML
	Tris(cyclopentadienyl)yttrium(III) (YCp <sub>3</sub> )		99.9% trace metals basis	491969-1G 491969-5G
	Yttrium(III) acetylacetonate hydrate		99.95% trace metals basis	438790-5G



Atomic Number of Base Material	Name (Synonym)	Structure	Purity	Prod. No.
40 Zirconium	Tetrakis(diethylamido)zirconium(IV)		≥99.99% trace metals basis	453153-5ML
	Zirconium(IV) diisopropoxidebis(2,2,6,6-tetramethyl-3,5-heptanedionate)		≥99.99%	494151-25G
	Zirconium tetrakis(2,2,6,6-tetramethyl-3,5-heptanedionate)		≥99.99%	478865-5G 478865-25G
42 Molybdenum	Molybdenumhexacarbonyl	Mo(CO) <sub>6</sub>	≥99.9% trace metals basis	577766-5G 577766-25G
44 Ruthenium	Triruthenium dodecacarbonyl		99%	245011-1G 245011-5G
46 Palladium	Palladium(II) acetylacetonate		99%	209015-1G 209015-5G
49 Indium	Indium(III) acetylacetonate		≥99.99% trace metals basis	I3300-1G I3300-5G
50 Tin	Tetrakis(dimethylamido)tin(IV)		99.9% trace metals basis	698431-1G
51 Antimony	Triphenylantimony(III)		99%	T81809-25G T81809-100G
	Tris(dimethylamido)antimony(III)		99.99% trace metals basis	553972-25ML
52 Tellurium	Tellurium tetrabromide	TeBr <sub>4</sub>	99.999% trace metals basis	464589-5G
	Tellurium tetrachloride	TeCl <sub>4</sub>	99%	205338-5G 205338-25G 205338-100G
56 Barium	Barium bis(6,6,7,7,8,8,8-heptafluoro-2,2-dimethyl-3,5-octanedionate)		99.99% trace metals basis	495174-5G 495174-25G
57 Lanthanum	Tris(cyclopentadienyl)lanthanum(III) (LaCp <sub>3</sub> )		99.9% trace metals basis	493597-1G
	Tris(tetramethylcyclopentadienyl)lanthanum(III)		99.9% trace metals basis	513180-1G
63 Europium	Tris(tetramethylcyclopentadienyl)europium(III)		99.9%	511374-1G

Atomic Number of Base Material	Name (Synonym)	Structure	Purity	Prod. No.
64 Gadolinium	Tris(cyclopentadienyl)gadolinium(III) (GdCp <sub>3</sub> )		99.9% trace metals basis	492566-1G 492566-5G
	Tris(tetramethylcyclopentadienyl)gadolinium(III)		99.9% trace metals basis	511366-1G
65 Terbium	Tris(cyclopentadienyl)terbium(III) (TbCp <sub>3</sub> )		99.9% trace metals basis	554006-5G
	Tris(tetramethylcyclopentadienyl)terbium(III)		99.9%	525065-1G
68 Erbium	Erbium(III) tris(2,2,6,6-tetramethyl-3,5-heptanedionate)		≥99.9% trace metals basis	434078-1G
	Tris(cyclopentadienyl)erbium(III) (ErCp <sub>3</sub> )		99.99% trace metals basis	491918-5G
69 Thulium	Tris(cyclopentadienyl)thulium(III) (TmCp <sub>3</sub> )		99.9% trace metals basis	553980-5G
70 Ytterbium	Tris(cyclopentadienyl)ytterbium(III)		99.9% trace metals basis	492434-1G 492434-5G
72 Hafnium	Bis(trimethylsilyl)amidohafnium(IV) chloride		≥95% ≥99.99% trace metals basis	J100005-5G
	Hafnium(IV) <i>tert</i> -butoxide		99.99% trace metals basis (purity excludes ~2,000 ppm zirconium.)	445541-5G
	Tetrakis(diethylamido)hafnium(IV)		99.99%	455202-10G
73 Tantalum	Pentakis(dimethylamino)tantalum(V)		99.9%	496863-5G
	Tris(diethylamido)(ethylimido)tantalum(V)		99.99% trace metals basis	517836-5ML
	Tris(diethylamido)( <i>tert</i> -butylimido)tantalum(V)		99% ≥99.99% trace metals basis	521280-5ML
	Tris(ethylmethylamido)( <i>tert</i> -butylimido)tantalum(V)		≥95% (CP) ≥99.99% trace metals basis	J100043-5G
74 Tungsten	Tungsten hexacarbonyl	W(CO) <sub>6</sub>	≥99.9% trace metals basis	472956-5G 472956-25G
	Tungsten(0) pentacarbonyl- <i>N</i> -pentylnitrile		99%	535567-5ML

# Complex Hydrides: A New Category of Solid-state Lithium Fast-ion Conductors



Motoaki Matsuo,<sup>1</sup> Hiroyuki Oguchi,<sup>1,2</sup> Hideki Maekawa,<sup>2</sup>  
Hitoshi Takamura,<sup>2</sup> Shin-ichi Orimo<sup>1\*</sup>  
<sup>1</sup>Institute for Materials Research, Tohoku University  
Katahira 2-1-1, Sendai, 980-8577, Japan  
<sup>2</sup>Graduate School of Engineering, Tohoku University  
Aramaki Aza Aoba 6-6-02, Sendai, 980-8579, Japan  
\*Email: orimo@imr.tohoku.ac.jp

## Introduction

Research and development of solid-state lithium fast-ion conductors is crucial because they can be potentially used as solid electrolytes in all-solid-state batteries, which may solve the safety and energy-density related issues of conventional lithium-ion batteries that use liquid (farmable organic) electrolytes. So far, a wide variety of inorganic lithium fast-ion conductors of oxides,<sup>1,2</sup> nitrides<sup>3</sup> and sulfides<sup>4,5</sup> have been extensively studied because they have an advantage in high ion conductivity [ $>10^{-3}$  S/cm at room temperature (RT)] as well as high lithium ion transport number ( $\sim 1$ ). Further efforts continue to overcome various barriers to practical realization, for example very high grain boundary resistance.

Lithium fast-ion conduction was discovered in  $\text{LiBH}_4$  (Aldrich Prod. No. 686026) in 2007.  $\text{LiBH}_4$  has not only high ion conductivity but also the following advantages for the solid electrolyte in lithium-ion batteries: (1) extremely low grain boundary resistance, (2) high electrochemical stability up to at least 5 V (vs  $\text{Li}^+/\text{Li}$ ) at 390 K, (3) extremely low polarization to metallic electrodes, (4) commercial availability and (5) suitability for various material processing techniques, including mechanical milling, heat treatment, impregnation and vapor deposition. This article reviews the fast-ion conduction in  $\text{LiBH}_4$  and its derivatives ( $\text{LiBH}_4\text{-LiI}$  and  $\text{LiBH}_4\text{-LiNH}_2$  systems), as a new category of solid-state lithium fast-ion conductors.

## Lithium Fast-ion Conduction in $\text{LiBH}_4$

Complex hydrides are generally expressed as  $M(M'H_n)$ , where  $M$  is a metal cation and  $(M'H_n)$  represents a complex anion such as  $(\text{NH}_2)^-$ ,  $(\text{BH}_4)^-$  and  $(\text{AlH}_4)^-$ .  $\text{LiBH}_4$  is a representative complex hydride, and has recently attracted great interest as a potential candidate for advanced hydrogen storage materials because of its high hydrogen density.  $\text{LiBH}_4$  undergoes a structural transition at about 390 K from the orthorhombic

low-temperature (LT) phase to the hexagonal high-temperature (HT) phase. Our study of microwave irradiation-induced rapid hydrogen desorption suggested that  $\text{LiBH}_4$  might become conductive in the HT phase, although it is an insulator in both the LT phase and the HT phase with large band gap of about 7 eV.

Therefore, we systematically examined the lithium ion conductivity of  $\text{LiBH}_4$  by an arc complex impedance method and  $^7\text{Li}$  NMR measurement.<sup>6</sup>

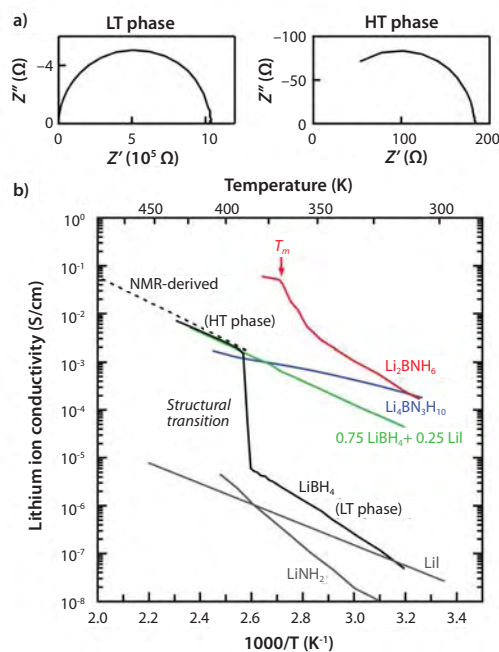


**Figure 1.** Electrical properties of  $\text{LiBH}_4$  and its derivatives. (a) Typical impedance plots for the LT phase and the HT phase of  $\text{LiBH}_4$  obtained using lithium-metal electrodes. (b) Temperature dependence of the lithium ion conductivity. The melting temperature of  $\text{Li}_2\text{BNH}_6$ , 368 K, is indicated as  $T_m$ .

Figure 1(a) shows the temperature dependence of the electrical conductivity of  $\text{LiBH}_4$  as determined from the impedance plots shown in Figure 1(b). The impedance plots of both the LT phase and the HT phase show only a single arc, indicating that the response arising from the grain boundary is not observed, although the pelletized sample used for the impedance measurement was prepared simply by pressing powder  $\text{LiBH}_4$  without subsequent sintering. The conductivities of the LT phase are very low, in the range of  $10^{-8}$  to  $10^{-6}$  S/cm, and the value linearly increases with increasing temperature. At about 390 K, the transition temperature, the conductivity drastically increases by three orders of magnitude. As a result, the HT phase exhibits high conductivity of the order of  $10^{-3}$  S/cm. The activation energies for conduction are evaluated to be 0.69 eV and 0.53 eV for the LT and HT phases, respectively.

In order to confirm whether the high electrical conductivity of  $\text{LiBH}_4$  in the HT phase is due to the lithium fast ion mobility,  $^7\text{Li}$  NMR was measured. Figure 2 shows the  $^7\text{Li}$  NMR spectra at selected temperatures.

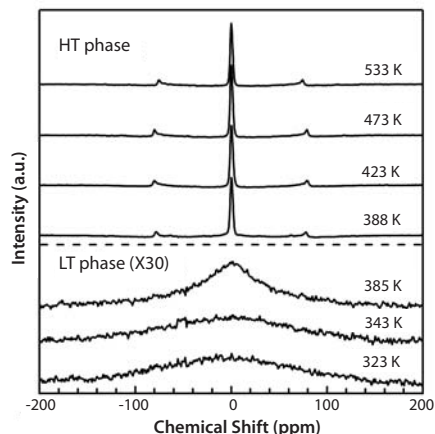


Figure 2.  $^7\text{Li}$  NMR spectra of  $\text{LiBH}_4$  at selected temperatures.

The shapes of the spectra drastically change at the structural transition temperature. In the LT phase (<385 K), only broad and small peaks are observed. On the contrary, in the HT phase (>388 K), each spectrum shows a central sharp line and two satellite lines. The decrease in the line width of the central line indicates the motional narrowing caused by the lithium fast ion motion in the HT phase. Furthermore, Figure 1 also shows the NMR-derived conductivity estimated by the Nernst-Einstein equation using the correlation times obtained by the temperature dependence of the spin-lattice relaxation time  $T_1$ . Clearly, the NMR data show a fairly good agreement with that measured by the impedance method. Thus, we concluded the charge carrier must be  $\text{Li}^+$  ions; the HT phase is a lithium fast-ion conductor.

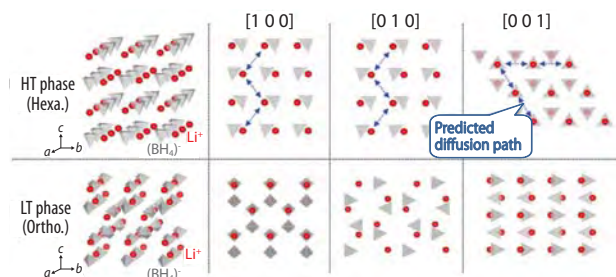


Figure 3. Crystal structures of  $\text{LiBH}_4$  in orthorhombic LT phase (bottom) and hexagonal HT phase (top). Red sphere and gray tetrahedrons show  $\text{Li}^+$  and  $(\text{BH}_4)^-$  ions, respectively. Blue arrowed lines show the predicted diffusion path.

As shown in Figure 3, the characteristic feature of the HT structure is that both  $\text{Li}^+$  ions and  $(\text{BH}_4)^-$  ions line up along the  $a$  axis and the  $b$  axis such that there is no  $(\text{BH}_4)^-$  ion between  $\text{Li}^+$  ions and vice versa. This arrangement may enable  $\text{Li}^+$  ions to migrate along these directions. Detailed studies using first-principles molecular dynamics simulations<sup>7</sup> and high-pressure impedance measurements<sup>8</sup> are now under way.

## Enhanced Conductivity of the Complex Hydrides Derived from $\text{LiBH}_4$

The lithium fast-ion conduction in  $\text{LiBH}_4$  could potentially aid the development of solid electrolytes in all-solid-state batteries. From an application point of view, however, it is highly desirable to enhance the conductivity at room temperature (RT). For that purpose, next, we tried materials design of fast-ion conductors of complex hydrides. As a typical example, we have investigated the  $\text{LiBH}_4\text{-LiI}$  and  $\text{LiBH}_4\text{-LiNH}_2$  systems with different concepts.

### Stabilization of the HT Phase in the $\text{LiBH}_4\text{-LiI}$ System<sup>9-11</sup>

We assumed that the stabilization of the HT phase should significantly improve the conductivity at RT, and the substitution of  $(\text{BH}_4)^-$  ion by  $\text{I}^-$  ion, of which ion radius (2.20 Å) is larger than that of  $(\text{BH}_4)^-$  ion (2.05 Å), might be effective for that purpose because it has been reported that alkali-metal borohydrides  $M\text{BH}_4$  ( $M = \text{Na}, \text{K}, \text{Rb}$  and  $\text{Cs}$ ) with longer distances between neighboring  $(\text{BH}_4)^-$  ions exhibit the lower transition temperatures.<sup>12</sup>

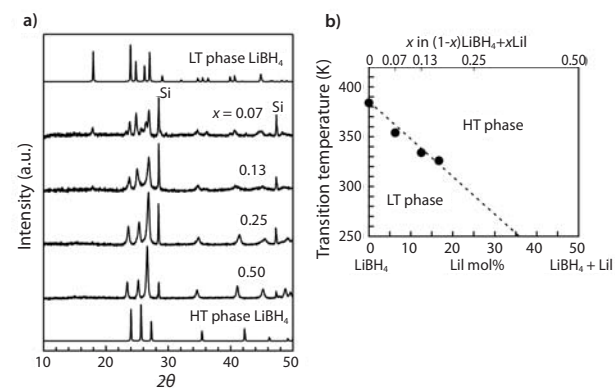


Figure 4. (a) XRD profiles of  $(1-x)\text{LiBH}_4 + x\text{LiI}$  synthesized by mechanical milling ( $x = 0.07 - 0.50$ ) and (b) structural transition temperatures determined by DSC as a function of value  $x$  (top axis) and "LiI mol %" (bottom axis).

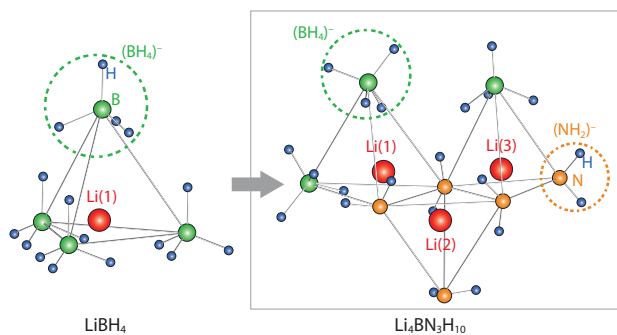
Figure 4(a) shows the x-ray diffraction (XRD) profiles of  $(1-x)\text{LiBH}_4 + x\text{LiI}$  synthesized by mechanical milling. The profiles gradually change from the LT phase to the HT phase with increasing amounts of LiI (Aldrich Prod. No. 518018). For  $x = 0.25$  and  $0.5$ , only the peaks corresponding to the HT phase are observed with being shifted to lower angle, indicating the substitution of  $(\text{BH}_4)^-$  ion by  $\text{I}^-$  ion. The transition temperatures determined by differential scanning calorimetry (DSC), shown in Figure 4(b), clearly show the stabilization feature of the HT phase depending on the molar ratio of LiI. The vibrational properties measured by spatially resolved Raman spectroscopy demonstrated the importance of anharmonic effects in the structural transformation in this system.<sup>13</sup>

Figure 1 also shows the result of the ion conductivity measurements for  $x = 0.25$ . The conductivity follows the Arrhenius behavior throughout the measured temperature range without the abrupt change observed for  $\text{LiBH}_4$  due to the structural transition. As expected, we achieved the increase in the conductivity at RT by 3 orders of magnitude without high conductivity of the HT phase decreased. We also confirmed that the substitution of  $(\text{BH}_4)^-$  ion by  $\text{Cl}^-$  ion leads to the enhanced conductivity.<sup>14</sup>



## Double Complex Anions in the $\text{LiBH}_4\text{-LiNH}_2$ System<sup>15</sup>

The  $\text{LiBH}_4\text{-LiNH}_2$  system has been studied from the viewpoint of developing hydrogen storage materials, and two phases,  $\text{Li}_2\text{BNH}_6$  and  $\text{Li}_4\text{BN}_3\text{H}_{10}$ , have been known to exist. As shown in **Figure 5**, both  $\text{Li}_2\text{BNH}_6$  and  $\text{Li}_4\text{BN}_3\text{H}_{10}$  have different configuration of anions from  $\text{LiBH}_4$ :  $\text{Li}^+$  ions are tetrahedrally coordinated by combinations of  $(\text{BH}_4)^-$  and  $(\text{NH}_2)^-$ . The  $\text{LiBH}_4\text{-Li}$  system showed the ion conductivity is affected by configuration of anions to a great degree, which made us get interested in these local structures.



**Figure 5.** Local atomic structures of  $\text{LiBH}_4$  (left) and  $\text{Li}_4\text{BN}_3\text{H}_{10}$  (right). Red, green, orange and blue solid spheres show Li, B, N and H, respectively.  $\text{Li}_4\text{BN}_3\text{H}_{10}$  has multiple occupation sites for  $\text{Li}^+$  ions while  $\text{LiBH}_4$  has only one site.

The conductivity measurements indicate that  $\text{Li}_2\text{BNH}_6$  has fast-ion conductivity of  $2 \times 10^{-4}$  S/cm at RT, which is 4 and 5 orders of magnitude higher than those of the host hydrides  $\text{LiBH}_4$  and  $\text{LiNH}_2$ , respectively, and the conductivity monotonically increases upon heating (**Figure 1**). The activation energy significantly decreases at around 368 K from 0.56 eV (303–348 K) to 0.24 eV (above 368 K) due to melting. The total ion conductivity reaches up to  $6 \times 10^{-2}$  S/cm at the highest temperature measured 378 K.  $\text{Li}_2\text{BNH}_6$  could be a good ionic liquid electrolyte as well as a solid electrolyte.  $\text{Li}_4\text{BN}_3\text{H}_{10}$  also exhibits high ion conductivity of  $2 \times 10^{-4}$  S/cm even at RT. The activation energy is evaluated to be 0.26 eV. It is noteworthy that this value is less than half those in  $\text{Li}_2\text{BNH}_6$  before melting and  $\text{LiBH}_4$ , indicating that  $\text{Li}_4\text{BN}_3\text{H}_{10}$  has higher lithium ion mobility. This feature was also confirmed by  $^7\text{Li}$  NMR, reflecting the different configuration of anions.<sup>15</sup>

## Future Perspective

In this short review, we have introduced the lithium fast-ion conduction in  $\text{LiBH}_4$  and its derivatives. We have recently elucidated that  $(\text{NH}_2)^-$ -based and  $(\text{AlH}_4)^-$ -based complex hydrides are also lithium ion conductors. The further research and development should provide new lithium ion conductors and new phenomena characteristic for complex hydrides.

Additionally, our group is currently focusing on the following subjects in order to demonstrate all-solid-state batteries using complex hydride solid electrolytes:

- (1) Search for non-oxide cathode materials
- (2) Synthesis of thin-film  $\text{Li}_4\text{BN}_3\text{H}_{10}$

Among the complex hydrides introduced in this review,  $\text{Li}_4\text{BN}_3\text{H}_{10}$  is the most promising candidate for solid electrolyte because it has the highest conductivity and the lowest activation energy. Thin-film  $\text{Li}_4\text{BN}_3\text{H}_{10}$  would allow the fabrication of thin-film lithium ion batteries, such as graphite/thin-film  $\text{Li}_4\text{BN}_3\text{H}_{10}$ /above-mentioned new cathode, for micro electromechanical system (MEMS).

## Acknowledgments

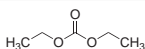
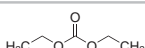
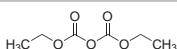
Support for this work by KAKENHI (22760529, 18GS0203, 21360314 and 21246100) is gratefully acknowledged.

## References

- (1) Aono, H.; Sugimoto, E.; Sadaoka, Y.; Imanaka, N.; Adachi, G. *J. Electrochem. Soc.* **1993**, *140*, 1827.
- (2) Inaguma, Y.; Liqun, C.; Itoh, M.; Nakamura, T.; Uchida, T.; Ikuta, H.; Wakihara, M. *Solid State Commun.* **1993**, *86*, 689.
- (3) Rabenau, A. *Solid State Ionics* **1982**, *6*, 277.
- (4) Kanno, R.; Murayama, M. *J. Electrochem. Soc.* **2001**, *148*, A742.
- (5) Ito, K.; Hayashi, A.; Morimoto, H.; Tatsumisago, M.; Minami, T. *Chem. Mater.* **2002**, *14*, 2444.
- (6) Matsuo, M.; Nakamori, Y.; Orimo, S.; Maekawa, H.; Takamura, H. *Appl. Phys. Lett.* **2007**, *91*, 224103.
- (7) Ikeshoji, T.; Tsuchida, E.; Ikeda, K.; Matsuo, M.; Li, H.-W.; Kawazoe, Y.; Orimo, S. *Appl. Phys. Lett.* **2009**, *95*, 221901.
- (8) Takamura, H.; Kuronuma, Y.; Maekawa, H.; Matsuo, M.; Orimo, S. *Solid State Ionics* (in press).
- (9) Maekawa, H.; Matsuo, M.; Takamura, H.; Ando, M.; Noda, Y.; Karahashi, T.; Orimo, S. *J. Am. Chem. Soc.* **2009**, *131*, 894.
- (10) Oguchi, H.; Matsuo, M.; Hummelshøj, J. S.; Vegge, T.; Nørskov, J. K.; Sato, T.; Miura, Y.; Takamura, H.; Maekawa, H.; Orimo, S. *Appl. Phys. Lett.* **2009**, *94*, 141912.
- (11) Miyazaki, R.; Karahashi, T.; Kumatani, N.; Noda, Y.; Ando, M.; Takamura, H.; Matsuo, M.; Orimo, S.; Maekawa, H. *Solid State Ionics* **2010** (online).
- (12) Stephensen, C. C.; Rice, D. W.; Stockmayer, W. H. *J. Chem. Phys.* **1955**, *23*, 1960.
- (13) Borgschulte, A.; Gremaud, R.; Kato, S.; Stadie, P.; Remhof, A.; Züttel, A.; Matsuo, M.; Orimo, S. *Appl. Phys. Lett.* **2010**, *97*, 031916.
- (14) Matsuo, M.; Takamura, H.; Maekawa, H.; Li, H.-W.; Orimo, S. *Appl. Phys. Lett.* **2009**, *94*, 084103.
- (15) Matsuo, M.; Remhof, A.; Martelli, P.; Caputo, R.; Ernst, M.; Miura, Y.; Sato, T.; Oguchi, H.; Maekawa, H.; Takamura, H.; Borgschulte, A.; Züttel, A.; Orimo, S. *J. Am. Chem. Soc.* **2009**, *131*, 16389.

## Battery Electrolyte Materials: Ionic Liquids and Solvents

For a complete list of available electrolytes for alternative energy, please visit [aldrich.com/energy](http://aldrich.com/energy)

Name	Structure	Purity	Prod. No.
Hexafluorophosphoric acid solution	HPF <sub>6</sub>	70% solution based on hydrolysis products and PF <sub>6</sub> <sup>-</sup> basis 60% solution based on PF <sub>6</sub> <sup>-</sup> only basis, ~65 wt. % in H <sub>2</sub> O	200956-25G 200956-500G
Acetonitrile	CH <sub>3</sub> CN	99%	110086-5ML 110086-1L 110086-2.5L 110086-4L
Acetonitrile	CH <sub>3</sub> CN	≥99.5%	154601-1L 154601-2L
1,2-Dimethoxyethane, anhydrous	H <sub>3</sub> CO-CH <sub>2</sub> -CH <sub>2</sub> -OCH <sub>3</sub>	99.5%	259527-100ML 259527-12X100ML 259527-1L 259527-6X1L 259527-2L 259527-10L 259527-18L
Thionyl chloride		≥99%	230464-5ML 230464-100ML 230464-1L
Thionyl chloride		97%	320536-1L
Thionyl chloride solution		2.0 M in methylene chloride	293121-100ML 293121-800ML
Dimethyl sulfite		99%	108618-100G
Ethyl methyl sulfone		97%	709980-5G
Dimethyl carbonate		99%	D152927-500ML D152927-1L D152927-100G D152927-500G D152927-2.5KG D152927-19KG
Diethyl carbonate, anhydrous		≥99%	517135-100ML 517135-1L
Diethyl carbonate		99%	D91551-250ML D91551-1L D91551-2.5L D91551-4L D91551-18L
Diethyl pyrocarbonate		97%	159220-5G 159220-25G 159220-100G
Tetrahydrofuran, anhydrous		≥99.9%	186562-100ML 186562-12X100ML 186562-1L 186562-6X1L 186562-2L 186562-4X2L 186562-18L 186562-20L 186562-200L-P1
Ethylene carbonate		98%	E26258-100G E26258-500G E26258-3KG



Name	Structure	Purity	Prod. No.
Propylene carbonate, anhydrous		99.7%	310328-100ML 310328-500ML 310328-1L 310328-2L
Propylene carbonate		99.7%	414220-1L 414220-2L
1-Ethyl-3-methylimidazolium tetrachloroaluminate, for energy applications		-	724424-5G
1-Butyl-3-methylimidazolium thiocyanate, for energy applications		≥95%	724408-5G
1-Butyl-3-methylimidazolium methanesulfonate, for energy applications		-	724394-5G
1,2-Dimethyl-3-propylimidazolium bis(trifluoromethylsulfonyl)imide		-	724416-1G
Methyl-trioctylammonium bis(trifluoromethylsulfonyl)imide, for energy applications		-	724432-1G

## Lithium Salts for Energy Applications: Hydrides and Amides

For a complete list of available materials for hydrogen storage, please visit [aldrich.com/hydrogenstorage](http://aldrich.com/hydrogenstorage)

Name	Structure	Purity	Prod. No.
Lithium amide, hydrogen-storage grade	$\text{LiNH}_2$	-	686050-10G
Lithium amide	$\text{LiNH}_2$	95%	213217-5G 213217-100G 213217-500G
Lithium borohydride, hydrogen-storage grade	$\text{LiBH}_4$	≥90%	686026-10G
Lithium borohydride	$\text{LiBH}_4$	≥90%	222356-1G 222356-10G 222356-50G
Lithium borodeuteride	$\text{LiBD}_4$	≥95%	685917-500MG



## Lithium Salts for Energy Applications: Halogenides

Name	Structure	Physical Form	Purity	Prod. No.
Lithium bromide	LiBr	powder and chunks	≥99.995% trace metals basis	229733-25G 229733-125G
Lithium bromide	LiBr	beads	≥99.9%	483982-5G 483982-25G
Lithium bromide	LiBr	beads	99.999% trace metals basis	429465-5G 429465-25G
Lithium bromide	LiBr	beads	≥99.9% trace metals basis	449873-25G 449873-100G
Lithium bromide hydrate	LiBr • xH <sub>2</sub> O	solid	99.999% trace metals basis	451754-10G
Lithium chloride	LiCl	powder	≥99.99% trace metals basis	203637-10G 203637-50G 203637-100G
Lithium chloride	LiCl	beads	99.998% trace metals basis	429457-5G 429457-25G
Lithium chloride	LiCl	beads	≥99.9% trace metals basis	449881-10G 449881-50G
Lithium chloride hydrate	LiCl • H <sub>2</sub> O	crystalline	≥99.99% trace metals basis	298328-25G 298328-100G
Lithium chloride hydrate	LiCl • H <sub>2</sub> O	crystals and lumps	≥99.0%, AT (calc. based on dry substance)	62486-25G 62486-100G
Lithium fluoride	LiF	powder	-	237965-100G 237965-1KG
Lithium fluoride	LiF	powder	99.995%	669431-50G
Lithium fluoride	LiF	fused (pieces)	99.995%	668052-10G 668052-25G 668052-100G
Lithium fluoride	LiF	powder	≥99.98% trace metals basis	203645-5G 203645-25G
Lithium fluoride	LiF	powder and chunks	≥99.99% trace metals basis	449903-2G 449903-10G 449903-50G
Lithium hexafluoroarsenate (V)	LiAsF <sub>6</sub>	powder	98%	308315-10G
Lithium hexafluorophosphate	LiPF <sub>6</sub>	powder	≥99.99% trace metals basis	450227-5G 450227-25G
Lithium hexafluorophosphate	LiPF <sub>6</sub>	powder	98%	201146-5G 201146-25G
Lithium iodide	LiI	crystalline powder	99.9% trace metals basis	518018-10G 518018-50G
Lithium iodide	LiI	beads	99%	218219-10G 218219-50G 218219-250G 218219-6X250G
Lithium iodide	LiI	beads	99.999% trace metals basis	450952-5G 450952-25G
Lithium iodide	LiI	beads	99.99% trace metals basis	439746-5G 439746-25G
Lithium iodide hydrate	LiI • xH <sub>2</sub> O	powder and chunks	99.999% trace metals basis	452327-5G 452327-25G 452327-100G
Lithium iodide hydrate	LiI • xH <sub>2</sub> O	solid	98%	223816-5G 223816-100G 223816-500G

# Inert Atmosphere Glove Boxes

Sigma-Aldrich® offers a wide range of Plas-Labs® glove boxes for oxygen and moisture-sensitive applications

## Features

- Clear, one-piece acrylic top and molded base section
- Double-layered gaskets for a reliable, airtight seal
- 8 in. ports with Hypalon® glove provide easy access to glove box
- Transparent transfer chamber with adjustable vacuum gauge



## Nitrogen Dry Box

- Drying train removal without disturbing internal atmosphere
- Two vacuum/pressure pumps to speed purging
- Fluorescent light system with illuminated controls

### Single-station Model

Z562920	AC input 120 V
Z563285	AC input 240 V, Euro plug
Z562939	AC input 240 V, UK plug

### Multi-station Model

Z562947	AC input 120 V
Z563293	AC input 240 V, Euro plug
Z562955	AC input 240 V, UK plug

## Basic Glove Box

- Three-tier suspended clear acrylic shelves
- White leveling tray for transferring the transfer chamber
- Four purge valves



### Single-station Model

Z563013	AC input 120 V
Z563307	AC input 240 V, Euro plug
Z563021	AC input 240 V, UK plug

### Multi-station Model

Z563048	AC input 120 V
Z563315	AC input 240 V, Euro plug
Z563056	AC input 240 V, UK plug

## Eliminating Static from Glove Boxes

The anti-static ionizer from Plas-Labs is an effective way to eliminate troublesome static in plastic glove boxes.

- Compact footprint
- Virtually maintenance free

### Anti-static Ionizer

Z563064	AC input 120 V
Z563072	AC input 240 V, UK plug
Z563323	AC input 240 V, Euro plug

For more information about the full range of glove boxes or to place an order, please go to [sigma-aldrich.com](http://sigma-aldrich.com)

Plas-Labs is a registered trademark of Plas-Labs, Inc. Hypalon is a registered trademark of E.I. du Pont de Nemours & Co., Inc.



# Mechanochemical Effect of Severe Plastic Deformations: Metal Alloys, Hydrides and Molecular Solids



Jacques Huot<sup>1</sup>, Viktor Balema<sup>2</sup>

<sup>1</sup>Hydrogen Research Institute, Université du Québec à Trois-Rivières, Trois-Rivières, 3351, des Forges Blvd., PO Box 500, QC, G9A 5H7, Canada

<sup>2</sup>Aldrich Materials Science, Sigma-Aldrich Corporation  
6000 N. Teutonia Ave, Milwaukee, WI, 53209, USA

Email: jacques.huot@uqtr.ca, viktor.balema@sial.com

## Introduction

Hydrogen, as an alternative to a traditional energy vector such as oil, coal and natural gas, has been the focus of research and development efforts in all technologically advanced countries of the world. It is strongly believed that a hydrogen-based economy can resolve energy-related problems and slow down global climate change. Hydrogen can be produced from a variety of renewable sources, is non-toxic and as an energy carrier, extremely environmentally benign. However, despite apparent benefits, an immediate incorporation of hydrogen into the world economy faces serious challenges. Although it is routinely used by chemical and refining industries, the cost of hydrogen storage and delivery is too high for the majority of energy applications. Yet, storing hydrogen in solids, metal alloys and hydrides offers a unique opportunity for its convenient and safe use in a variety of portable and stationary applications.

This article gives a brief overview of an experimental approach that is used for the preparation and processing of metallic hydrogen storage materials. The approach employs the chemical effect of plastic deformations for nano-scale design and modification of hydrogen absorbing metals and alloys.<sup>1</sup>

The paper specifically focuses on the methods which introduce severe plastic deformation (SPD) into metal alloys and metal hydrides, and compares SPD to another mechanical processing technique—ball milling. Finally, it also highlights a possible role of plastic deformations in mechanically induced transformations of hydrogen-rich molecular solids, which recently attracted a great deal of interest.<sup>2</sup>

## Severe Plastic Deformations in the Preparation of Metal Hydrides

Severe plastic deformations can be introduced into metallic and intermetallic systems using several relatively simple but very efficient techniques such as: equal channel angular pressing (ECAP), high-pressure torsion (HPT) or cold rolling (CR). Similar to high-energy ball milling,<sup>2</sup> these techniques were initially developed for the forming and processing of metals but proved to be efficient tools for the preparation and modification of hydrogen storage materials.

**Equal Channel Angular Pressing (ECAP)** introduces severe plastic deformations into the material by forcing a sample (billet) through a die consisting of two channels of equal cross-section, which intersect at an angle between 90° and 120°. <sup>3</sup> (Figure 1)

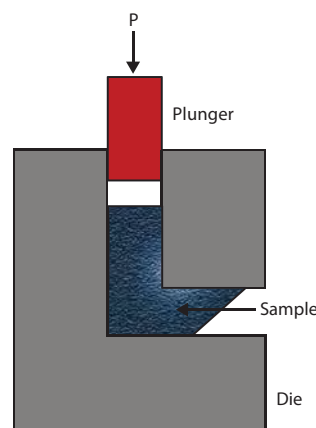
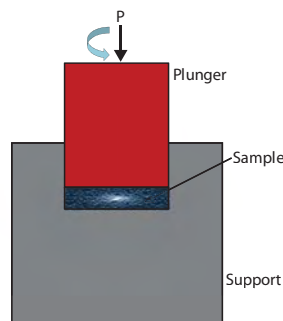


Figure 1. Schematic illustration of Equal Channel Angular Pressing (ECAP).

Since the billet assumes the form and cross-section of the die, it can be repeatedly processed to increase the microstrain and reduce the size of crystallites in the material. In addition, by simply rotating the billet between successive pressings, different slip systems could be activated in the sample. ECAP efficiently processes metals as it enables the production of porosity-free materials with average crystallite sizes between 2  $\mu\text{m}$  and 100 nm in substantial quantities with lower concentration of impurities and at a lower cost than conventional ball milling.<sup>4</sup> ECAP has been directly compared to ball milling by Skripnyuk et al., who studied the kinetics and thermodynamics of hydrogen sorption in commercial ZK60 alloy (94.34 wt.% Mg, 4.95 wt.% Zn, 0.71 wt.% Zr) processed by ECAP and/or ball milling.<sup>5</sup> Although ECAP proved to be quite efficient in enhancing hydrogen absorption and desorption ability of the alloy, the highest effect was achieved when it was combined with high-energy milling. In another similar study, the investigation of a commercial magnesium alloy AZ31 (96 wt.% Mg, 3 wt.% Al, 1 wt.% Zn) processed by ECAP between 423 K and 573 K,<sup>6</sup> also revealed that the optimal hydrogen absorption and desorption parameters of AZ31 were obtained when three different mechanical processing techniques [ECAP, cold rolling (CR), and high-energy ball milling] were combined. Thus, it seems safe to assume that the full advantage of ECAP can be taken if it is combined with other processing techniques, rather than when it is used alone.



In the case of **High Pressure Torsion (HPT)** processing, a powder or thin film material is subjected to a high pressure and a concurrent torsion straining (**Figure 2**).



**Figure 2.** Schematic illustration of High Pressure Torsion (HPT).

As HPT is generally restricted to small (sub-gram scale) samples, it is mainly used to evaluate fundamental effects of SPD in solid materials. One such study was performed by Kusadome, et al. on  $\text{MgNi}_2$  alloy,<sup>7</sup> which does not usually absorb hydrogen. However, after the HPT processing introduced a substantial strain in the material, it became a weak hydrogen absorber (0.1 wt.%) with hydrogen accumulating in grain boundaries of the alloy.<sup>7</sup> In another experiment, Lima, et al. observed a substantial improvement in the hydrogen sorption kinetics of a Mg-Fe powder mixture processed by HPT.<sup>8</sup> They noted that the hydrogenation and dehydrogenation of the processed samples did not affect the preferential (002) orientation of the Mg phase, i.e., the material retained the microstructure imposed by HPT.

Similarities between HPT and ball milling were evidenced in the recent work by Leiva, et al. who detected the formation of a metastable  $\gamma\text{-MgH}_2$  phase and a substantial reduction of crystallite sizes in magnesium hydride, while using HPT to consolidate the metal hydride powder.<sup>9</sup> Previously, the formation of  $\gamma\text{-MgH}_2$  upon mechanical processing was chiefly associated with high-energy ball milling.<sup>10</sup>

In **Cold Rolling (CR)** a sheet of metal is introduced between rollers where it is compressed and squeezed through the roller (**Figure 3**).

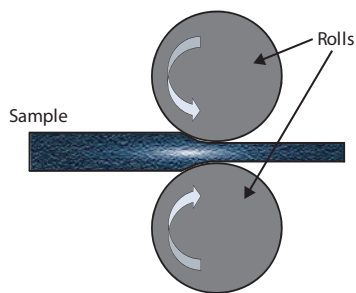


**Figure 3.** Schematic illustration of Cold Rolling (CR).

The amount of strain introduced by CR determines the hardness and other properties of the finished product.<sup>11</sup> Usually, rolling is classified according to the processing temperature as compared with the metal re-crystallization temperature:

- Hot rolling (HR) is the process carried out at a temperature exceeding the re-crystallization temperature of the rolled material
- Cold rolling (CR) is usually performed at a temperature below the re-crystallization temperature

The effect of cold rolling on hydrogen sorption properties of hydrogen storage alloys has been studied in detail.<sup>12-14</sup> Zhang et al., investigated the effect of deformations on hydrogen sorption behavior of Ti-based alloys.<sup>12,13</sup> In their experiments, deformations in the material were generated by cold rolling or compression. It turned out that the first hydrogenation (activation) of the cold-rolled alloys was much faster than

that of the unprocessed (*as-quenched*) samples. Unfortunately, this positive effect of CR disappeared after a few hydrogenation/dehydrogenation cycles as the material returned to its initial state. Couillaud, et al. investigated the effect of a multiple CR on the hydrogen absorption properties of  $\text{TiV}_{1.6}\text{Mn}_{0.4}$  and compared it to a high-energy ball milling.<sup>14</sup> The study revealed that cold rolling and ball milling had a similar effect—both techniques caused the reduction of crystallite sizes and the lattice parameters of the alloy without changing its crystal structure. S. Kikuchi's group investigated the effect of CR on the hydrogen storage ability of various Mg-based multi-component alloys.<sup>15</sup> For the Mg-Ni system, they found that a Mg-Ni laminated composite, subjected to an additional heat treatment, transforms into the intermetallic alloy  $\text{Mg}_2\text{Ni}$ , which upon exposure to hydrogen can be converted into the metal hydride  $\text{Mg}_2\text{NiH}_4$ . The composition  $2\text{Mg}+\text{Ni}$  was also studied by Pedneault, et al., who investigated the effect of cold rolling on the electrochemical properties of the processed alloys.<sup>16</sup> They found that a combination of CR with an additional heat treatment is a promising approach to the preparation of nanostructured metal hydrides. The nanocrystalline  $\text{Mg}_2\text{Ni}$  prepared by cold rolling showed electrochemical performance similar to that of nanocrystalline  $\text{Mg}_2\text{Ni}$  powder made by high-energy ball milling from magnesium and nickel. In another example, the laminated Mg-Pd composite materials demonstrate faster activation and better air resistance than the ball-milled samples of the same stoichiometry.<sup>17</sup>

## Cold Rolling of Magnesium and Magnesium Hydride

Similar to HPT and high-energy ball milling, cold rolling of  $\text{MgH}_2$  (**Aldrich Prod. No. 683043**) facilitates the formation of the metastable  $\gamma\text{-MgH}_2$  phase in magnesium hydride, thus indicating that CR should be at least as energetic as other processing techniques discussed above.<sup>9</sup>

In recent experiments, J. Huot's group compared the effects of CR and high-energy ball milling on the hydrogen absorption properties of magnesium hydride. **Figure 4** shows the hydrogen absorption kinetics of an *as-received* magnesium hydride and the samples obtained by ball-milling (for 30 min) or cold rolling (for 5 times).

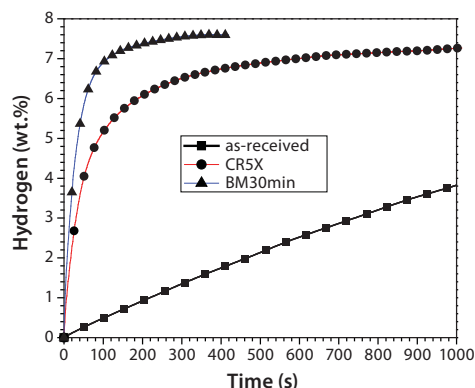


**Figure 4.** Hydrogen absorption kinetic at 623 K and under 2 MPa hydrogen pressure of  $\text{MgH}_2$  in *as-received*, cold rolled five times (CR5X), and mechanically milled (BM30mins) states.

The untreated magnesium hydride has very slow absorption/desorption kinetics and ball milling for 30 minutes considerably enhances it. Remarkably, the cold rolled sample demonstrates similar kinetics to that of the ball milled material, despite the fact that the rolling was performed in air while the ball-milling was carried out under argon to prevent the material's oxidation during processing. Thus, cold rolling offers a simple and economical way to modify magnesium, compared to the more expensive and time consuming high-energy ball milling.

It can be expected that the severe strain associated with severe plastic deformations in hydride forming metals, such as magnesium and its alloys, could generate a variety of defects that serve as a nucleation point for the hydride phase. To test this hypothesis, cold rolled magnesium and a commercial magnesium alloy AZ91 (~92% of Mg and ~8% of Al with minor additions of Zn, Mn and Si) were investigated. Each sample was folded and rolled 50 times then exposed to hydrogen. As a reference, a pure untreated magnesium powder was exposed to hydrogen under the same conditions. **Figure 5** shows the hydrogen absorption (activation) curves collected at 623 K under the hydrogen pressure of 20 bar.

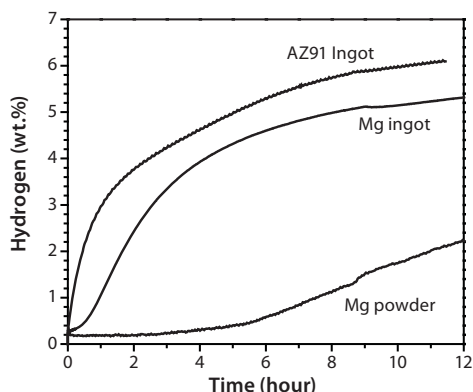


**Figure 5.** First hydrogenation (activation) curves of magnesium powder, cold rolled magnesium (Mg ingot) and cold rolled commercial alloy (AZ91 ingot). Activation was performed at 623 K under a hydrogen pressure of 20 bar.

As expected, cold-rolled activated samples demonstrate considerably higher ability to absorb hydrogen in the activation cycle than the untreated magnesium powder. In addition, the rolled samples start to absorb immediately after the exposure to hydrogen, while the absorption by the untreated powder has a long incubation time.

## Mechanically Induced Transformations of Molecular Solids

The experimental results presented above clearly demonstrate that severe plastic deformations introduced into metallic materials by Equal Channel Angular Pressing, High Pressure Torsion or Cold Rolling significantly enhance the ability of metals to interact with each other and/or with hydrogen. In other words, severe plastic deformations facilitate mechanically induced chemical transformations in metals and metal hydrides and allow the synthesis of metal alloys and hydride phases ranging from solid solutions to binary and complex metal hydrides (such as  $Mg_2NiH_4$  or  $MgH_2$ ). It is also safe to assume that the effect of SPD is similar to that of mechanical milling with the major difference being that SPD techniques may offer a less expensive and more scalable way to carry out mechanically activated processes.

To further understand the relationship between SPD and ball milling, it may be helpful to look into the changes that occur in a solid material trapped between colliding balls or balls and container walls during a high-energy ball-mill process. Once trapped between the balls, solid material is subjected to an external pressure causing a sequence of deformations (**Figure 6**) which starts with reversible elastic deformations followed by irreversible plastic deformations, such as shear and twist deformations. As pressure increases, the latter becomes quite severe and lead to the fracture and/or amorphization of the material.<sup>2</sup>

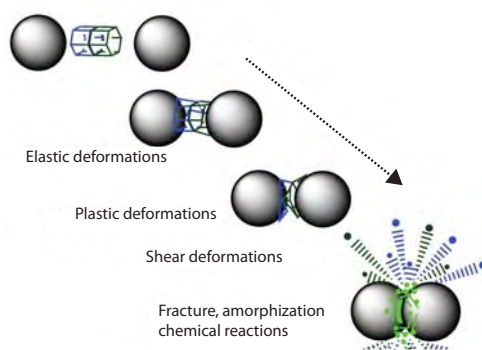


**Figure 6.** Deformations in the material trapped between two colliding balls during ball milling.

Thus, the character of deformations caused by ball milling are quite similar to those introduced by SPD techniques, which may explain the similarities between these mechanical processing techniques.

For high-energy ball milling, an additional factor to consider is the high-pressure generated within the material trapped between the colliding balls and the walls of the milling container. The pressure in such contact areas may reach several GPa,<sup>2</sup> making it sufficient to facilitate pressure-driven chemical transformations in metals, ionic hydrides or molecular (organic) solids. However, in a number of cases, very similar chemical reactions are known to occur under conditions that may or may not generate high-pressure spots, but certainly introduce severe plastic deformations into the processed materials. For example, the high-energy ball milling of a mixture of solid phosphonium salts and solid organic aldehydes in the presence of potassium carbonate enables the solvent-free Wittig reaction (**Figure 7**).<sup>18</sup>

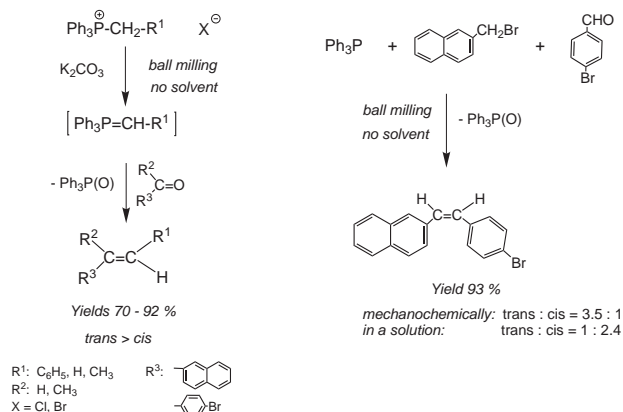


**Figure 7.** The mechanically induced solvent-free Wittig reaction.

Initially, the high-pressure generated in the material during ball milling was held responsible for the effect.<sup>2</sup> However, further experiments revealed that the use of ball milling is not crucial for this mechanochemical process and the solvent-free Wittig reactions can be run by grinding the reactants with pestle and mortar,<sup>19</sup> which shouldn't generate the ultra-high pressure in the material but is certainly a source of severe plastic deformations similar to those introduced by CR or HPT.



## Conclusion

This review of the effects of SPD on the properties of solid materials clearly demonstrates the efficiency of SPD in the preparation and modification of metallic, ionic and molecular solids. For magnesium and magnesium alloys specifically, SPD can enhance the hydrogen storage ability of these materials and improves their hydrogen storage capacities on the first hydrogenation/dehydrogenation (activation) cycle. A similar effect of SPD is also observed for the cold-rolled magnesium hydride. It seems quite feasible that the severe plastic deformations may be also responsible for the chemical effect of mechanical processing of molecular solids, including such complex multi-step transformations as the mechanically-induced, solvent-free Wittig reaction. Amongst the various SPD techniques, cold rolling is arguably the easiest to scale-up to an industrial level. Therefore, it may supersede high-energy milling for the production of nanocrystalline metallic and ionic materials and can likely also be applied to the conversion of molecular (organic) solids. The studies into the application of SPD in materials chemistry of solid materials are at the very early stages of their development and a substantial additional effort is needed to exploit the full potential of this mechanochemical technique.

## Acknowledgments

We would like to thank Y. Turcotte, J. Lang and Dr. S. Amira at Université du Québec à Trois-Rivières for help in the study of the effect of SPD.

## References

- Valiev, R. Z.; Islamgaliev, R. K.; Alexandrov, I. V. *Prog. Mater. Sci.* **2000**, *45*, 103.
- Balema, V. P., *Material Matters*, **2007**, Vol. 2, No. 1, 16.
- Skripnyuk, V. M.; Rabkin, E.; Estrin, Y.; Lapovok, R. *Int. J. Hydrogen Energy* **2009**, *34*, 6320.
- Langdon, T. G. *Rev. Adv. Mater. Sci.* **2006**, *13*, 6.
- Skripnyuk, V. M.; Rabkin, E.; Estrin, Y.; Lapovok, R. *Acta Mater.* **2004**, *52*, 405.
- Leiva, D. R.; Fruchart, D.; Bacia, M.; Girard, G.; Skryabina, N.; Villela, A. C. S.; Miraglia, S.; Santos, D. S.; Botta, W. J. *Int. J. Mater. Res.* **2009**, *100*, 1739.
- Kusadome, Y.; Ikeda, K.; Nakamori, Y.; Orimo, S.; Horita, Z. *Scripta Mater.* **2007**, *57*, 751.
- Lima, G. F.; Jorge, A. M.; Kiminami, C. S.; Botta, W. J.; Bolfarini, C. *Severe Plastic Deformation of Mg-Fe Powders to Produce Bulk Hydrides*, In 13th International Conference on Rapidly Quenched and Metastable Materials, Dresden, Germany, August 24-29, 2008; Schultz, L.; Eckert, J.; Battezzati, L.; Stoica, M., Eds.; IOP Publishing Ltd: Bristol, 2009.
- Leiva, D. R.; Jorge, A. M.; Ishikawa, T. T.; Hout, J.; Fruchart, D.; Miraglia, S.; Kiminami, C. S.; Botta, W. J. *Adv. Eng. Mater.* **2010**, *12*, 786.
- Huot, J.; Swainson, I.; Schulz, R. *Ann. Chim.- Sci. Mat.* **2006**, *31*, 135.
- Jiang, W. H.; Atzom, M. *Appl. Phys. Lett.* **2005**, *86*, 151916.
- Zhang, L. T.; Ito, K.; Vasudevan, V. K.; Yamaguchi, M. *Acta Mater.* **2001**, *49*, 751.
- Zhang, L. T.; Ito, K.; Vasudevan, V. K.; Yamaguchi, M. *Mater. Sci. Eng., A* **2002**, *329*, 362.
- Couillaud, S.; Enoki, H.; Amira, S.; Bobet, J. L.; Akiba, E.; Huot, J. *J. Alloys Compd.* **2009**, *484*, 154.
- Ueda, T. T.; Tsukahara, M.; Kamiya, Y.; Kikuchi, S. *J. Alloys Compd.* **2004**, *386*, 253.
- Pedneault, S.; Huot, J.; Roué, L. *J. Power Sources* **2008**, *185*, 566.
- Takeichi, N.; Tanka, K.; Tanaka, H.; Ueda, T. T.; Kamiya, Y.; Tsukahara, M.; Miyamura, H.; Kikuchi, S. *J. Alloys Compd.* **2007**, *446*, 543.
- Balema, V. P.; Wiench, J. W.; Pruski, M.; Pecharsky, V. L. *J. Amer. Chem. Soc.* **2002**, *124*, 6244.
- Leung, S. H.; Angel, S. A. *J. Chem. Ed.* **2004**, *81*, 1492.

## Metal Hydrides for Hydrogen Storage Applications

For a complete list of available metal hydrides for hydrogen storage, please visit [aldrich.com/hydrogenstorage](http://aldrich.com/hydrogenstorage)

Atomic Number of Base Material	Name	Structure	Purity	Prod. No.
3	Lithium aluminum hydride, hydrogen-storage grade	LiAlH <sub>4</sub>	-	686034-10G
	Lithium aluminum hydride, reagent grade	LiAlH <sub>4</sub>	95%	199877-10G 199877-25G 199877-100G 199877-1KG
	Lithium hydride	LiH	95%	201049-5G 201049-10G 201049-100G 201049-500G
11	Sodium aluminum hydride, hydrogen-storage grade	NaAlH <sub>4</sub>	93%	685984-10G
	Sodium aluminum hydride solution	NaAlH <sub>4</sub>	1 M in THF	698865-1L
	Sodium borohydride, hydrogen-storage grade	NaBH <sub>4</sub>	98%	686018-10G
12	Magnesium borohydride	Mg(BH <sub>4</sub> ) <sub>2</sub>	95%	715247-1G
	Magnesium hydride, hydrogen-storage grade	MgH <sub>2</sub>	-	683043-10G
20	Calcium borohydride	Ca(BH <sub>4</sub> ) <sub>2</sub>	-	695254-1G
	Calcium hydride	CaH <sub>2</sub>	99.99% trace metals basis	497355-2G 497355-10G
	Calcium hydride	CaH <sub>2</sub>	99.9% trace metals basis	558257-10G
22	Titanium(II) hydride	TiH <sub>2</sub>	98%	209279-100G 209279-500G
	Titanium(II) hydride, hydrogen-storage grade	TiH <sub>2</sub>	-	686069-1G
40	Zirconium(II) hydride	ZrH <sub>2</sub>	99%	208558-1G 208558-100G



## Metal Alloys for Hydrogen Storage and Battery Applications

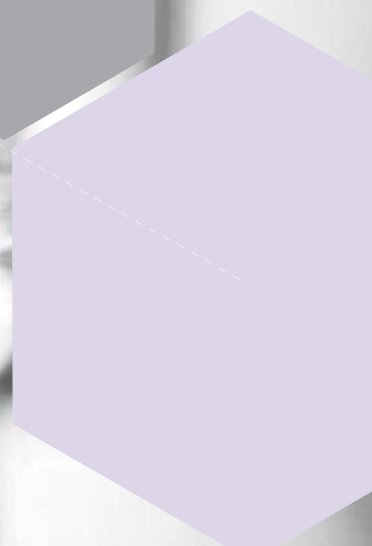
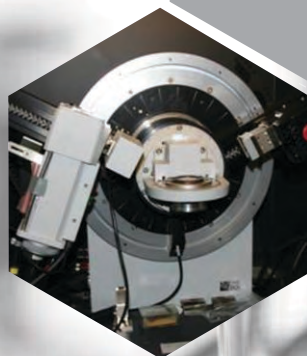
For a complete list of available metal alloys for hydrogen storage, please visit [aldrich.com/hydrogenstorage](http://aldrich.com/hydrogenstorage)

Name	Composition	Prod. No.
Lanthanum-nickel alloy	LaNi <sub>5</sub>	685933-10G
Lanthanum-nickel-cobalt alloy	La <sub>2</sub> Co <sub>1</sub> Ni <sub>9</sub>	685968-10G
Mischmetal-nickel alloy	(Ce, La, Nd, Pr)Ni <sub>5</sub>	685976-10G
Titanium-manganese alloy	TiMn <sub>2</sub>	685941-10G
Yttrium-Nickel alloy, YNi <sub>5</sub>	YNi <sub>5</sub>	693928-5G
Zirconium-iron alloy	ZrFe <sub>2</sub>	693812-1G
Zirconium-scandium-iron alloy	Fe <sub>10</sub> Sc <sub>1</sub> Zr <sub>4</sub>	693804-1G

## High Purity Magnesium

For a complete list of available magnesium materials for hydrogen storage, please visit [aldrich.com/hydrogenstorage](http://aldrich.com/hydrogenstorage)

Name	Purity	Form	Prod. No.
Magnesium	99.5% trace metals basis	powder	465666-50G 465666-250G
Magnesium	≥99%	powder	253987-5G 253987-100G 253987-1KG
Magnesium	≥99%	powder	13112-100G 13112-6X100G 13112-500G 13112-1KG 13112-6X1KG 13112-25KG
Magnesium	≥99.0%, KT	grit	63045-250G-F
Magnesium	≥99.0%, KT	grit	63040-250G-F 63040-1KG-F
Magnesium	99.98% trace metals basis	chips	254118-250G 254118-1KG
Magnesium	99.998% trace metals basis	dendritic pieces	474754-5G 474754-25G
Magnesium	99.99% trace metals basis	dendritic pieces	465992-5G 465992-25G
Magnesium	99.95% trace metals basis	turnings	403148-50G 403148-250G
Magnesium	≥99.5%	turnings	63035-250G-F 63035-1KG-F
Magnesium	≥99.5% Mg basis	ribbon	13103-25G 13103-6X25G
Magnesium	≥99% trace metals basis	ribbon	266302-25G
Magnesium	≥99.9% trace metals basis	rod	299405-10G
Magnesium, hydrogen activated	≥99.5%	powder	682896-10G



# Hard Materials Center of Excellence

The Hard Materials Center of Excellence at Urbana, Illinois, addresses a variety of technologies ranging from Alternative Energy and Electronics to Bio-Medical applications. Research and development capabilities available at the Center enable development and custom manufacturing of high-purity metals, alloys, salts, advanced ceramics and other hard materials for both academic and industrial customers.

## The Hard Materials Center of Excellence offers:

- Conventional and mechanical alloying
- Forming and shaping of metals
- Purification of metals by vacuum distillation
- Beading of salts
- Purification of high-purity salts by crystallization
- Controlled/inert-gas atmosphere
- Full analytical suite including XRD, particle size analysis, ICP-MS/OES, DSC/TGA, elemental analysis, NMR and more



To inquire about our custom capabilities, please contact us at [matsci@sial.com](mailto:matsci@sial.com)

## Sigma-Aldrich® Worldwide Offices

### Argentina

Free Tel: 0810 888 7446  
Tel: (+54) 11 4556 1472  
Fax: (+54) 11 4552 1698

### Australia

Free Tel: 1800 800 097  
Free Fax: 1800 800 096  
Tel: (+61) 2 9841 0555  
Fax: (+61) 2 9841 0500

### Austria

Tel: (+43) 1 605 81 10  
Fax: (+43) 1 605 81 20

### Belgium

Free Tel: 0800 14747  
Free Fax: 0800 14745  
Tel: (+32) 3 899 13 01  
Fax: (+32) 3 899 13 11

### Brazil

Free Tel: 0800 701 7425  
Tel: (+55) 11 3732 3100  
Fax: (+55) 11 5522 9895

### Canada

Free Tel: 1800 565 1400  
Free Fax: 1800 265 3858  
Tel: (+1) 905 829 9500  
Fax: (+1) 905 829 9292

### Chile

Tel: (+56) 2 495 7395  
Fax: (+56) 2 495 7396

### China

Free Tel: 800 819 3336  
Tel: (+86) 21 6141 5566  
Fax: (+86) 21 6141 5567

### Czech Republic

Tel: (+420) 246 003 200  
Fax: (+420) 246 003 291

### Denmark

Tel: (+45) 43 56 59 00  
Fax: (+45) 43 56 59 05

### Finland

Tel: (+358) 9 350 9250  
Fax: (+358) 9 350 92555

### France

Free Tel: 0800 211 408  
Free Fax: 0800 031 052  
Tel: (+33) 474 82 28 88  
Fax: (+33) 474 95 68 08

### Germany

Free Tel: 0800 51 55 000  
Free Fax: 0800 64 90 000  
Tel: (+49) 89 6513 0  
Fax: (+49) 89 6513 1160

### Hungary

Ingyenes telefonszám: 06 80 355 355  
Ingyenes fax szám: 06 80 344 344  
Tel: (+36) 1 235 9063  
Fax: (+36) 1 269 6470

### India

**Telephone**  
Bangalore: (+91) 80 6621 9400  
New Delhi: (+91) 11 4358 8000  
Mumbai: (+91) 22 4087 2364  
Hyderabad: (+91) 40 4015 5488  
Kolkata: (+91) 33 4013 8000

### Fax

Bangalore: (+91) 80 6621 9550  
New Delhi: (+91) 11 4358 8001  
Mumbai: (+91) 22 2579 7589  
Hyderabad: (+91) 40 4015 5466  
Kolkata: (+91) 33 4013 8016

### Ireland

Free Tel: 1800 200 888  
Free Fax: 1800 600 222  
Tel: (+353) 402 20370  
Fax: (+353) 402 20375

### Israel

Free Tel: 1 800 70 2222  
Tel: (+972) 8 948 4100  
Fax: (+972) 8 948 4200

### Italy

Free Tel: 800 827 018  
Tel: (+39) 02 3341 7310  
Fax: (+39) 02 3801 0737

### Japan

Tel: (+81) 3 5796 7300  
Fax: (+81) 3 5796 7315

### Korea

Free Tel: (+82) 80 023 7111  
Free Fax: (+82) 80 023 8111  
Tel: (+82) 31 329 9000  
Fax: (+82) 31 329 9090

### Malaysia

Tel: (+60) 3 5635 3321  
Fax: (+60) 3 5635 4116

### Mexico

Free Tel: 01 800 007 5300  
Free Fax: 01 800 712 9920  
Tel: (+52) 722 276 1600  
Fax: (+52) 722 276 1601

### The Netherlands

Free Tel: 0800 022 9088  
Free Fax: 0800 022 9089  
Tel: (+31) 78 620 5411  
Fax: (+31) 78 620 5421

### New Zealand

Free Tel: 0800 936 666  
Free Fax: 0800 937 777  
Tel: (+61) 2 9841 0555  
Fax: (+61) 2 9841 0500

### Norway

Tel: (+47) 23 17 60 00  
Fax: (+47) 23 17 60 10

### Poland

Tel: (+48) 61 829 01 00  
Fax: (+48) 61 829 01 20

### Portugal

Free Tel: 800 202 180  
Free Fax: 800 202 178  
Tel: (+351) 21 924 2555  
Fax: (+351) 21 924 2610

### Russia

Tel: (+7) 495 621 5828  
Fax: (+7) 495 621 6037

### Singapore

Tel: (+65) 6779 1200  
Fax: (+65) 6779 1822

### Slovakia

Tel: (+421) 255 571 562  
Fax: (+421) 255 571 564

### South Africa

Free Tel: 0800 1100 75  
Free Fax: 0800 1100 79  
Tel: (+27) 11 979 1188  
Fax: (+27) 11 979 1119

### Spain

Free Tel: 900 101 376  
Free Fax: 900 102 028  
Tel: (+34) 91 661 99 77  
Fax: (+34) 91 661 96 42

### Sweden

Tel: (+46) 8 742 4200  
Fax: (+46) 8 742 4243

### Switzerland

Free Tel: 0800 80 00 80  
Free Fax: 0800 80 00 81  
Tel: (+41) 81 755 2828  
Fax: (+41) 81 755 2815

### United Kingdom

Free Tel: 0800 717 181  
Free Fax: 0800 378 785  
Tel: (+44) 1747 833 000  
Fax: (+44) 1747 833 313

### United States

Toll-Free: 800 325 3010  
Toll-Free Fax: 800 325 5052  
Tel: (+1) 314 771 5765  
Fax: (+1) 314 771 5757

### Vietnam

Tel: (+84) 3516 2810  
Fax: (+84) 6258 4238

### Internet

[sigma-aldrich.com](http://sigma-aldrich.com)



### Mixed Sources

Product group from well-managed forests, controlled sources and recycled wood or fiber  
[www.fsc.org](http://www.fsc.org) Cert no. SGSNA-COC-003338  
© 1996 Forest Stewardship Council



Enabling Science to  
Improve the Quality of Life

Order/Customer Service (800) 325-3010 • Fax (800) 325-5052  
Technical Service (800) 325-5832 • [sigma-aldrich.com/techservice](http://sigma-aldrich.com/techservice)  
Development/Custom Manufacturing Inquiries **SAFC**® (800) 244-1173  
Safety-related Information [sigma-aldrich.com/safetycenter](http://sigma-aldrich.com/safetycenter)

World Headquarters  
3050 Spruce St.  
St. Louis, MO 63103  
(314) 771-5765  
[sigma-aldrich.com](http://sigma-aldrich.com)